



A JWST Near- and Mid-infrared Nebular Spectrum of the Type Ia Supernova 2021aefx

Lindsey A. Kwok¹, Saurabh W. Jha¹, Tea Temim², Ori D. Fox³, Conor Larison¹, Yssavo Camacho-Neves¹, Max J. Brenner Newman¹, Justin D. R. Pierel³, Ryan J. Foley⁴, Jennifer E. Andrews⁵, Carles Badenes^{6,7}, Barnabas Barna^{8,9}, K. Azalee Bostroem^{10,44}, Maxime Deckers¹¹, Andreas Flörs¹², Peter Garnavich¹³, Melissa L. Graham¹⁴, Or Graur^{15,16}, Griffin Hosseinzadeh¹⁰, D. Andrew Howell^{17,18}, John P. Hughes¹, Joel Johansson¹⁹, Sarah Kendrew²⁰, Wolfgang E. Kerzendorf^{21,22}, Keiichi Maeda²³, Kate Maguire¹¹, Curtis McCully^{17,18}, John T. O'Brien²¹, Armin Rest^{3,24}, David J. Sand¹⁰, Melissa Shahbandeh³, Louis-Gregory Strolger³, Tamás Szalai^{8,25,26}, Chris Ashall²⁷, E. Baron^{28,29}, Chris R. Burns³⁰, James M. DerKacy²⁷, Tyco Mera Evans³¹, Alec Fisher³¹, Lluís Galbany^{32,33}, Peter Hoefflich³¹, Eric Hsiao³¹, Thomas de Jaeger³⁴, Emir Karamahmetoglu³⁵, Kevin Krisciunas^{36,37}, Sahana Kumar³¹, Jing Lu³¹, Justyn Maund³⁸, Paolo A. Mazzali^{39,40}, Kyle Medler³⁹, Nidia Morrell⁴¹, Mark M. Phillips⁴¹, Benjamin J. Shappee³⁴, Maximilian Stritzinger³⁵, Nicholas Suntzeff^{36,37}, Charles Telesco⁴², Michael Tucker^{43,45}, and Lifan Wang^{36,37}

¹ Department of Physics and Astronomy, Rutgers, the State University of New Jersey, 136 Frelinghuysen Road, Piscataway, NJ 08854-8019, USA
lindsey.kwok@physics.rutgers.edu

² Department of Astrophysical Sciences, Princeton University, 4 Ivy Lane, Princeton, NJ 08540-7219, USA

³ Space Telescope Science Institute, 3700 San Martin Drive, Baltimore, MD 21218-2410, USA

⁴ Department of Astronomy and Astrophysics, University of California, Santa Cruz, CA 95064-1077, USA

⁵ Gemini Observatory/NSF's NOIRLab, 670 North A'ohoku Place, Hilo, HI 96720-2700, USA

⁶ Department of Physics and Astronomy and Pittsburgh Particle Physics, Astrophysics and Cosmology Center (PITT PACC), University of Pittsburgh, 3941 Oara Street, Pittsburgh, PA 15260, USA

⁷ Institut de Ciències del Cosmos (ICCUB), Universitat de Barcelona (IEEC-UB), Martí i Guàrdia 1, E-08028 Barcelona, Spain

⁸ Department of Experimental Physics, Institute of Physics, University of Szeged, Dóm tér 9, Szeged, 6720 Hungary

⁹ Astronomical Institute, Academy of Sciences, Boční II 1401, Prague, Czech Republic

¹⁰ Steward Observatory, University of Arizona, 933 North Cherry Avenue, Tucson, AZ 85721-0065, USA

¹¹ School of Physics, Trinity College Dublin, The University of Dublin, Dublin 2, Ireland

¹² GSI Helmholtzzentrum für Schwerionenforschung, Planckstraße 1, D-64291 Darmstadt, Germany

¹³ Department of Physics and Astronomy, University of Notre Dame, Notre Dame, IN 46556, USA

¹⁴ DIRAC Institute, Department of Astronomy, University of Washington, Box 351580, U.W., Seattle, WA 98195, USA

¹⁵ Institute of Cosmology & Gravitation, University of Portsmouth, Dennis Sciama Building, Burnaby Road, Portsmouth PO1 3FX, UK

¹⁶ Department of Astrophysics, American Museum of Natural History, Central Park West and 79th Street, New York, NY 10024-5192, USA

¹⁷ Las Cumbres Observatory, 6740 Cortona Drive, Suite 102, Goleta, CA 93117-5575, USA

¹⁸ Department of Physics, University of California, Santa Barbara, CA 93106-9530, USA

¹⁹ Oskar Klein Centre, Department of Physics, Stockholm University, Albanova University Center, SE-106 91, Stockholm, Sweden

²⁰ European Space Agency, Space Telescope Science Institute, 3700 San Martin Dr., Baltimore, MD 21218, USA

²¹ Department of Physics and Astronomy, Michigan State University, East Lansing, MI 48824, USA

²² Department of Computational Mathematics, Science, and Engineering, Michigan State University, East Lansing, MI 48824, USA

²³ Department of Astronomy, Kyoto University, Kitashirakawa-Oiwake-cho, Sakyo-ku, Kyoto, 606-8502, Japan

²⁴ Department of Physics and Astronomy, The Johns Hopkins University, 3400 North Charles Street, Baltimore, MD 21218, USA

²⁵ ELKH-SZTE Stellar Astrophysics Research Group, H-6500 Baja, Szegedi út, Kt. 766, Hungary

²⁶ Konkoly Observatory, Research Centre for Astronomy and Earth Sciences, Eötvös Loránd Research Network (ELKH), Konkoly-Thege Miklós út 15-17, 1121 Budapest, Hungary

²⁷ Department of Physics, Virginia Tech, Blacksburg, VA 24061, USA

²⁸ Homer L. Dodge Department of Physics and Astronomy, University of Oklahoma, 440 W. Brooks, Rm 100, Norman, OK 73019-2061, USA

²⁹ Hamburger Sternwarte, Gojenbergsweg 112, D-21029 Hamburg, Germany

³⁰ Observatories of the Carnegie Institute for Science, 813 Santa Barbara Street, Pasadena, CA 91101-1232, USA

³¹ Department of Physics, Florida State University, 77 Chieftan Way, Tallahassee, FL 32306-4350, USA

³² Institute of Space Sciences (ICE, CSIC), Campus UAB, Carrer de Can Magrans, s/n, E-08193 Barcelona, Spain

³³ Institut d'Estudis Espacials de Catalunya, Gran Capità, 2-4, Edifici Nexus, Desp. 201, E-08034 Barcelona, Spain

³⁴ Institute for Astronomy, University of Hawai'i, 2680 Woodlawn Drive, Honolulu, HI 96822-1839, USA

³⁵ Department of Physics and Astronomy, Aarhus University, Ny Munkegade 120, DK-8000 Aarhus C, Denmark

³⁶ Department of Physics and Astronomy, Texas A&M University, 4242 TAMU, College Station, TX 77843, USA

³⁷ George P. and Cynthia Woods Mitchell Institute for Fundamental Physics & Astronomy, College Station, TX 77843, USA

³⁸ Department of Physics and Astronomy, University of Sheffield, Hicks Building, Hounsfield Road, Sheffield S3 7RH, UK

³⁹ Astrophysics Research Institute, Liverpool John Moores University, Liverpool, L3 5RF, UK

⁴⁰ Max-Planck Institute for Astrophysics, Garching, Germany

⁴¹ Carnegie Observatories, Las Campanas Observatory, Casilla 601, La Serena, Chile

⁴² Department of Astronomy, University of Florida, Gainesville, FL 32611 USA

⁴³ Center for Cosmology and Astroparticle Physics, The Ohio State University, 191 West Woodruff Avenue, Columbus, OH 43215, USA

Received 2022 October 31; revised 2023 January 10; accepted 2023 January 19; published 2023 February 8



Original content from this work may be used under the terms of the [Creative Commons Attribution 4.0 licence](https://creativecommons.org/licenses/by/4.0/). Any further distribution of this work must maintain attribution to the author(s) and the title of the work, journal citation and DOI.

⁴⁴ LSSTC Catalyst Fellow.

⁴⁵ CCAPP Fellow.

Abstract

We present JWST near-infrared (NIR) and mid-infrared (MIR) spectroscopic observations of the nearby normal Type Ia supernova (SN) SN 2021aefx in the nebular phase at +255 days past maximum light. Our Near Infrared Spectrograph (NIRSpec) and Mid Infrared Instrument observations, combined with ground-based optical data from the South African Large Telescope, constitute the first complete optical+NIR+MIR nebular SN Ia spectrum covering 0.3–14 μm . This spectrum unveils the previously unobserved 2.5–5 μm region, revealing strong nebular iron and stable nickel emission, indicative of high-density burning that can constrain the progenitor mass. The data show a significant improvement in sensitivity and resolution compared to previous Spitzer MIR data. We identify numerous NIR and MIR nebular emission lines from iron-group elements as well as lines from the intermediate-mass element argon. The argon lines extend to higher velocities than the iron-group elements, suggesting stratified ejecta that are a hallmark of delayed-detonation or double-detonation SN Ia models. We present fits to simple geometric line profiles to features beyond 1.2 μm and find that most lines are consistent with Gaussian or spherical emission distributions, while the [Ar III] 8.99 μm line has a distinctively flat-topped profile indicating a thick spherical shell of emission. Using our line profile fits, we investigate the emissivity structure of SN 2021aefx and measure kinematic properties. Continued observations of SN 2021aefx and other SNe Ia with JWST will be transformative to the study of SN Ia composition, ionization structure, density, and temperature, and will provide important constraints on SN Ia progenitor and explosion models.

Unified Astronomy Thesaurus concepts: [Supernovae \(1668\)](#); [Type Ia supernovae \(1728\)](#); [White dwarf stars \(1799\)](#)

1. Introduction

Type Ia supernovae (SN Ia) play an important role in astrophysics and cosmology, yet we still lack a detailed understanding of their progenitor systems and explosion physics. Nebular phase spectroscopy at late times (beyond about 100 days past maximum light; Bowers et al. 1997; Branch et al. 2008; Silverman et al. 2013; Friesen et al. 2014; Black et al. 2016) reveals the SN ejecta when they have expanded, allowing us to see to the innermost material. The observed flux is dominated by optically thin forbidden-line emission that directly probes the composition, density, temperature, and ionization structure of the ejecta, constraining models of thermonuclear explosions of a white dwarf (for a review, see Jerkstrand 2017).

At early times, most SN Ia flux is at optical wavelengths, but as the ejecta fade and cool to the nebular phase, the near-infrared (NIR) and mid-infrared (MIR) comprise a large fraction of the emission (Axelrod 1980; Fransson & Jerkstrand 2015). Nebular spectra have been obtained for hundreds of SNe Ia in the optical but far fewer in the ground-accessible NIR windows. There are only three SNe Ia to date with published nebular spectra in the MIR: one epoch each of SN 2003hv and SN 2005df, observed with Spitzer ($\lambda = 5\text{--}15 \mu\text{m}$ at spectral resolution $R \sim 90$; Gerardy et al. 2007); and four epochs of SN 2014J, observed from the ground with Gran Telescopio Canarias (GTC; $\lambda = 8\text{--}13 \mu\text{m}$ with $R \sim 60$; Telesco et al. 2015) at phases of +57, +81, +108, and +137 days. The atmospheric absorption and sky background limit the ground-based capabilities at these wavelengths. Spitzer was pushed to its sensitivity limits, and useful observations of these three SNe Ia were only possible because they were nearby ($d \sim 3.5$ Mpc for SN 2014J; Dalcanton et al. 2009; Goobar et al. 2014; and $d \lesssim 20$ Mpc for SN 2003hv and SN 2005df; Gerardy et al. 2007).

Nebular phase observations in the NIR and MIR provide unique and powerful constraints on models, including the density-dependent nucleosynthesis of intermediate-mass elements, radioactive iron-group elements, and stable iron-group elements (Gerardy et al. 2007; Dhawan et al. 2018; Diamond et al. 2018; Hoefflich et al. 2021). The JWST Near Infrared Spectrograph (NIRSpec; Jakobsen et al. 2022) and Mid Infrared Instrument (MIRI; Rieke et al. 2015; Wright et al. 2015)

provide access to a wider range of elemental and ionic species than the optical. Lines are also typically less blended in the infrared, making it easier to derive line fluxes and abundance estimates, as well as to infer the geometry of the emission region from the line profile shape (e.g., Jerkstrand 2017). Infrared spectra can also show evidence of dust formation in the SN ejecta and polycyclic aromatic hydrocarbon line features that reveal the local and galactic environment (Tielens 2005; Wang 2005; Rho et al. 2008; Johansson et al. 2017).

JWST, with its wider NIR and MIR wavelength coverage, better spectral resolution, and enormously increased sensitivity compared to previous facilities, will be transformative to our understanding of SNe Ia. Here we present the first NIR + MIR SN Ia spectrum from JWST, of SN 2021aefx, covering 0.6–14 μm . Our data include the previously unobserved 2.5–5 μm region and, combined with ground-based optical data, create a continuous optical + NIR + MIR SN Ia spectrum. This observation, taken as part of JWST cycle (1) General Observer (GO) program 2072 “See Through Supernovae” (PI: S. W. Jha), is the initial epoch of the first SN in a program to build a legacy, reference sample of JWST NIR + MIR nebular spectra of 9 white-dwarf (thermonuclear) SNe over three cycles. SN 2021aefx will also be the target of two epochs of data from the JWST cycle (1) GO program 2114 (PI: C. Ashall). Combined, these programs will observe SN 2021aefx in four epochs, providing the most comprehensive time series of nebular IR spectra for a SN Ia.

SN 2021aefx is a “normal” (see, e.g., Blondin et al. 2012) SN Ia that was discovered within hours of explosion by the Distance Less Than 40 Mpc (DLT40) survey (Tartaglia et al. 2018) on 2021 November 11.3 UT at $\alpha = 04^{\text{h}}19^{\text{m}}53^{\text{s}}.400$, and $\delta = -54^{\circ}56'53''.09$ (J2000; Hosseinzadeh et al. 2022). It is located in the nearby galaxy NGC 1566 with a distance of 18.0 ± 2.0 Mpc ($\mu = 31.28 \pm 0.23$ mag; Sabbi et al. 2018), and a redshift of $z = 0.005017$ (Allison et al. 2014), making it a bright target for our first observation with JWST.

SN 2021aefx peaked at an apparent magnitude of $B = 11.7$ mag ($M_B = -19.6$ mag; Hosseinzadeh et al. 2022) and exhibited an exceptionally high silicon velocity ($v \simeq 30,000 \text{ km s}^{-1}$) in the earliest spectrum (Bostroem et al. 2021). High-cadence intra-night observations of SN 2021aefx were

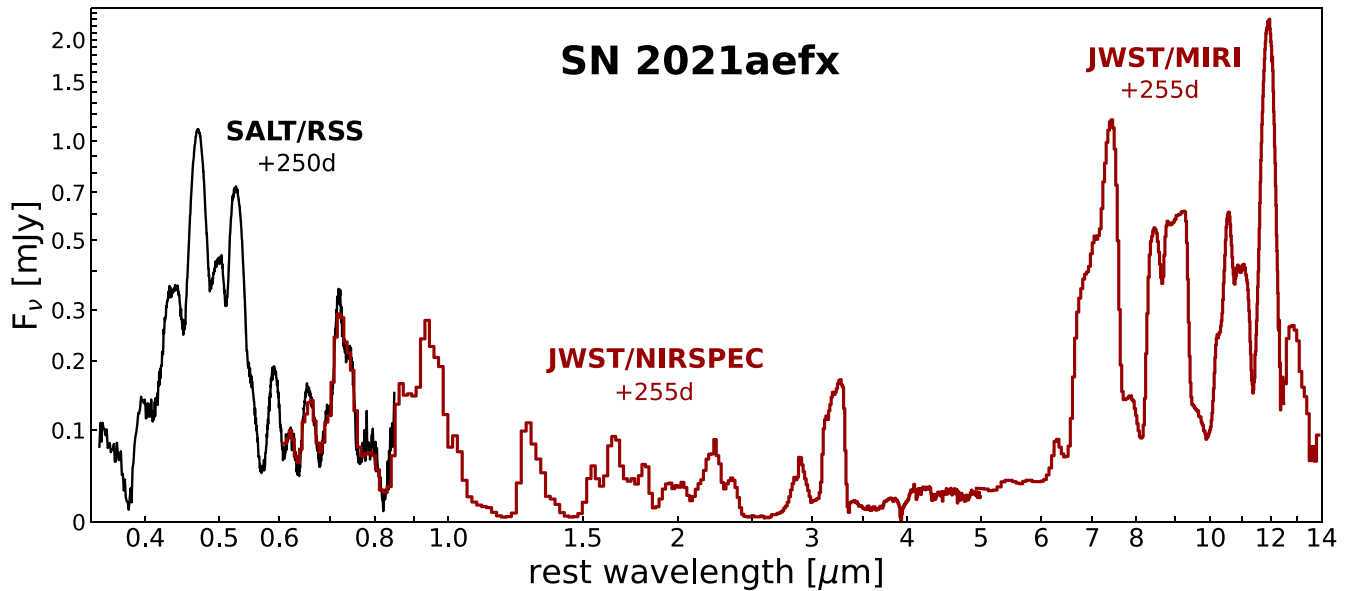


Figure 1. Combined optical + NIR + MIR spectrum of Type Ia SN 2021aefx in the nebular phase. The optical data are from SALT/RSS, and the NIR and MIR data were obtained with JWST/NIRSpec and JWST/MIRI, respectively. The optical flux is calibrated to ground-based photometry, and the MIRI flux is scaled to the MIRI F1000W photometry. The NIRSpec flux is unscaled from the JWST pipeline and matches up well to the optical and MIR. The spectrum has been dereddened and corrected for the host-galaxy redshift. For presentation purposes, the optical spectrum and the MIR spectrum past $12.5 \mu\text{m}$ have been rebinned to lower resolution. The flux axis uses a nonlinear (arcsinh) scale to better show all the features across a wide range of wavelength and F_ν . All subsequent spectra presented in the paper use a linear flux scale.

carried out by the Precision Observations of Infant Supernova Explosions (Burns et al. 2021; Ashall et al. 2022) and the DLT40 surveys, and additional multiwavelength follow-up photometry revealed an early light-curve excess, perhaps attributable to interaction between the ejecta and a nondegenerate companion star, interaction with circumstellar material, or the effect of an unusual nickel distribution (Hosseinzadeh et al. 2022). Part of the early light-curve evolution may also be explained by high and rapidly evolving ejecta velocities (Ashall et al. 2022). Aside from this peculiarity at the earliest epochs (which have rarely been probed), SN 2021aefx subsequently evolved into a normal SN Ia that would be included in cosmological samples. The evolution of SN 2021aefx has been closely followed by ground-based observatories and has generated significant interest in the SN community.

In Section 2, we detail our observations and data reduction; in Section 3, we identify optical, NIR, and MIR nebular emission lines in SN 2021aefx; and in Section 4, we present basic geometric line profile fits to the dominant spectral features. We discuss the implications of our results and conclude in Section 5.

2. Observations

We present the JWST spectrum of SN 2021aefx in Figure 1. We observed SN 2021aefx with both NIRSpec in the fixed slits (FS) spectroscopy mode (Birkmann et al. 2022; Jakobsen et al. 2022; Rigby et al. 2022) with the prism and MIRI in the low-resolution spectroscopy (LRS) mode (Kendrew et al. 2015, 2016; Rigby et al. 2022) on 2022 August 11.7 UT at a rest-frame phase of +254.9 days, relative to B -band maximum (59546.54 ± 0.03 MJD; Hosseinzadeh et al. 2022).

Our NIRSpec observations used the S200A1 ($0''.2$ wide \times $3''.3$ long) slit with the PRISM grating and CLEAR filter, and our MIRI observations used the LRS slit with the P750L

disperser. The combined wavelength coverage spans $0.6\text{--}14 \mu\text{m}$. Details of the observation settings are given in Table 1.

2.1. JWST Data Reduction

The data were reduced using the publicly available “jwst”⁴⁶ pipeline (version 1.8.0; Bushouse et al. 2022) routines for bias and dark subtraction, background subtraction, flat field correction, wavelength calibration, flux calibration, rectification, outlier detection, resampling, and spectral extraction. The final NIRSpec “stage 3” one-dimensional (1D) spectrum extracted by the automated pipeline, available on the Mikulski Archive for Space Telescopes (MAST),⁴⁷ was of sufficiently good quality that we did not rerun any portion of the pipeline. Unfortunately, the MIRI stage (3) 1D spectrum extracted by the automated pipeline, available on MAST, was noisy and unsuitable because the automated extraction aperture was not properly centered on the SN trace. Thus, we reextracted the spectrum by manually running stage (3) of the pipeline (calwebb_spec3) from the stage (2) (calwebb_spec2) data products, enforcing the correct extraction trace and aperture.

We identified an issue with the original MIRI/LRS slit wavelength calibration from the JWST pipeline that has been noted and confirmed by others and is under investigation (S. Kendrew & G. Sloan, private communication). Spectra of the candidate Herbig B[e] star VFTS 822, which exhibits hydrogen emission lines (Kalari et al. 2014), were taken as part of calibration programs JWST cycle (0) COM/MIRI 1259⁴⁸ (PI: S. Kendrew) and JWST cycle (1) CAL/MIRI 1530⁴⁹ (PI: S. Kendrew). From the data publicly available on the MAST archive, we measured wavelength centroids and uncertainties

⁴⁶ <https://github.com/spacetelescope/jwst>

⁴⁷ <https://mast.stsci.edu/portal/Mashup/Clients/Mast/Portal.html>

⁴⁸ <https://www.stsci.edu/jwst/phase2-public/1259.pdf>

⁴⁹ <https://www.stsci.edu/jwst/phase2-public/1530.pdf>

Table 1
JWST SN 2021aefx Observation Details

Setting	NIR	MIR
Instrument	NIRSpec	MIRI
Mode	FS	LRS
Wavelength Range	0.6 – 5.3 μm	5–14 μm
Slit	S200A1 (0 $''$ 2 \times 3 $''$ 3)	Slit
Grating and/or Filter	PRISM/CLEAR	P750L
$R = \lambda/\Delta\lambda$	~ 100	$\sim 40\text{--}250$
Subarray	FULL	FULL
Readout Pattern	NRSIRS2RAPID	FASTR1
Groups per Integration	5	134
Integrations per Exposure	2	2
Exposures (Nods)	3	2
Total Exposure Time	525 s	1493 s
Target Acquisition Exposure Time	4 s	89 s

for 12 H I emission line peaks in the data and matched them with their known rest wavelengths. We found significant offsets between the wavelengths from the pipeline calibration and the H I emission line wavelengths, with larger deviation at shorter wavelengths ($\sim 0.1 \mu\text{m}$ at the longest wavelengths, rising to $\sim 0.5 \mu\text{m}$ at the shortest wavelengths). We developed a custom wavelength solution correction that informed updates to the JWST pipeline by the MIRI Team. All MIRI/LRS slit data on MAST have been reprocessed by the new wavelength calibration, including the MIRI data of SN 2021aefx presented in this work. The inaccuracy in the wavelength calibration has been reduced to $\sim 0.02\text{--}0.05 \mu\text{m}$ (MIRI Team, private communication). We caution that the H I emission line peaks in the VFTS 822 data are weak and difficult to fit; full resolution of this wavelength calibration issue may require additional observations of other sources.

We measured MIRI F1000W photometry of SN 2021aefx from the LRS verification image (see Figure 2) with $F_\nu = 0.309 \pm 0.010$ mJy, corresponding to 17.67 ± 0.04 mag AB. The photometry was done on the F1000W data from the JWST pipeline using a 70% encircled energy aperture radius (4.3 pixels) and inner and outer sky radii of 6.063 and 10.19 pixels (and a corresponding aperture correction was also applied). Integrating the MIRI spectrum of the SN over the F1000W passband gave a flux that agreed with the measured photometry to within 2%. We applied a rescaling of the spectrum to match the photometry precisely. The NIRSpec spectrum does not have similarly measured photometry, but the pipeline spectrum matches both the optical and MIR spectra well, so we do not adjust its flux calibration.

To correct for extinction by dust, we use the Python `dust-extinction` package (v.1.1; Gordon et al. 2022). We deredden the NIRSpec spectrum out to $1.0 \mu\text{m}$ using the F19 model from Fitzpatrick et al. (2019) and the NIRSpec spectrum past $1.0 \mu\text{m}$ as well as the MIRI spectrum with the G21_MWavg model from Gordon et al. (2021). We correct for both the host-galaxy extinction of $E(B-V)_{\text{host}} = 0.097$ mag (Hosseinzadeh et al. 2022), and the Milky Way extinction of $E(B-V)_{\text{MW}} = 0.008$ mag (Schlafly & Finkbeiner 2011).

2.2. Optical Data

We obtained an optical nebular spectrum of SN 2021aefx with the Southern African Large Telescope (SALT) Robert Stobie Spectrograph (RSS; Smith et al. 2006) on 2022 August

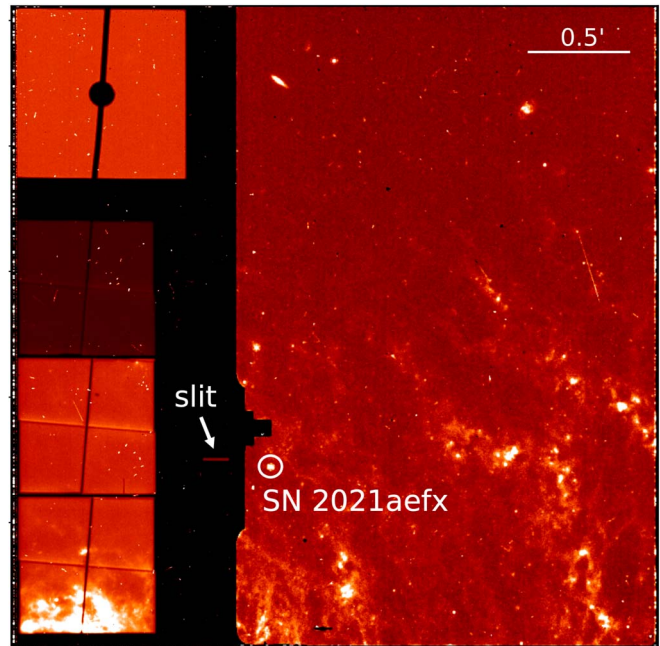


Figure 2. JWST MIRI F1000W verification image showing SN 2021aefx during target acquisition, before placement on the LRS slit. Part of the central region of the host galaxy, NGC 1566, can be seen in the bottom left corner; gas and dust features can be seen in the image on the right. Cosmic rays have been removed from the image.

7.1 UT (rest-frame phase of +250.3 days) using a $1''5$ longslit and the PG0900 grating in four tilt settings with a total exposure time of 2294 s. Using a custom pipeline based on standard Pyraf (Science Software Branch at STScI 2012) spectral reduction routines and the PySALT package (Crawford et al. 2010), we reduced the optical spectrum and removed cosmic rays, host-galaxy lines and continuum, and telluric absorption. We scaled the optical spectrum to observed contemporaneous $UBgVri$ photometry, obtained with the Sinistro cameras on Las Cumbres Observatory’s 1 m telescopes (Brown et al. 2013) and reduced automatically by the BANZAI (McCully et al. 2018) and `lcoqtsnpipe` (Valenti et al. 2016) pipelines, using the `speccal` module in the light-curve fitting package (Hosseinzadeh & Gomez 2020). Lastly, we applied a redshift correction to the host-galaxy rest frame and dereddened using the F19 model (Fitzpatrick et al. 2019) as above.

3. Line Identification

We identify nebular emission lines in the optical, NIR, and MIR spectra presented in this work using line identifications from the Atomic Line List⁵⁰, the Atomic-Infrared Space Observatory line list⁵¹; previous optical line identifications by Graham et al. (2022), Tucker et al. (2022), and Wilk et al. (2020); previous NIR line identifications by Diamond et al. (2018), Dhawan et al. (2018), Hoeflich et al. (2021), and Mazzali et al. (2015); previous MIR line identifications by Gerardy et al. (2007) and Telesco et al. (2015); and optical + NIR + MIR lines from models by Flörs et al. (2020).

In this work, we focus on line identifications for the $2.5\text{--}5 \mu\text{m}$ region in the NIR and the full $5\text{--}14 \mu\text{m}$ MIR. Candidate lines in these wavelength regions of interest were

⁵⁰ <https://www.pa.uky.edu/~peter/newpage/>

⁵¹ <https://www.mpe.mpg.de/ir/ISO/linelists/FSlines.html>

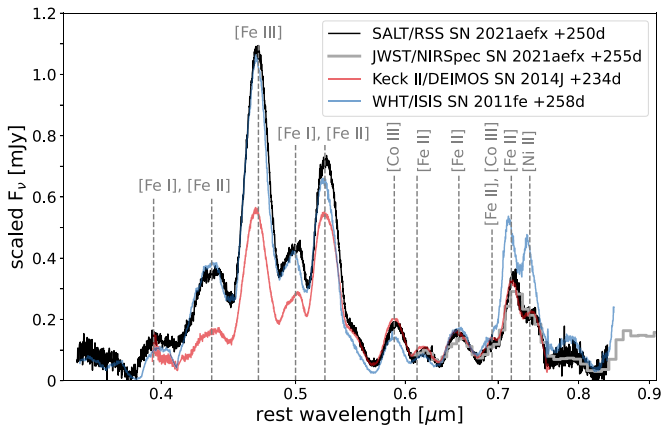


Figure 3. Optical line identifications for SN 2021aefx; only the most dominant species for each feature are shown. The optical spectrum (black) from SALT/RSS on 2022 August 7 at a rest-frame phase of +250 days is dominated by forbidden-line emission from iron-group elements. For comparison, we plot the JWST/NIRSpec spectrum (gray) on 2022 August 11 at +255 days, and the optical spectra of SN 2011fe (blue; Mazzali et al. 2015) and SN 2014J (red; Childress et al. 2015) at similar phase (+258 and +234 days, respectively). Phases are given with respect to B -band maximum, and all spectra have been dereddened.

narrowed down by selecting atomic species consistent with SN Ia abundance models (e.g., Nomoto et al. 1984; Thielemann et al. 1986; Fink et al. 2010; Pakmor et al. 2012; Seitzzahl et al. 2013), predicted strength of the forbidden-line transitions, and proximity to ground-state transitions.

Selected prominent optical lines are marked in Figure 3. The optical lines match closely with those presented by Graham et al. (2022), Tucker et al. (2022), and Wilk et al. (2020), and are dominated by blended emission lines from the iron-group elements: [Fe II], [Fe III], [Co III], and [Ni II]. We compare to an optical spectrum of SN 2011fe from Mazzali et al. (2015) using the William Herschel Telescope with the Intermediate-dispersion Spectrograph and Imaging System and dereddened by $E(B-V) = 0.023$ mag. We also compare to a spectrum of SN 2014J from Childress et al. (2015) taken with the Keck II telescope and the DEep Imaging Multi-Object Spectrograph, dereddened by $R_V = 1.4$, $E(B-V) = 1.2$ mag (Amanullah et al. 2014; Foley et al. 2014; Mazzali et al. 2015). The optical spectrum and line identification of SN 2021aefx closely matches that of SN 2011fe and SN 2014J, indicating that SN 2021aefx is representative of a typical SN Ia at about +250 days. The spectrum of SN 2011fe is slightly blueshifted compared to SN 2021aefx.

3.1. NIR Emission Lines

In Figure 4, we mark prominent lines in the JWST/NIRSpec spectrum of SN 2021aefx. Most of the lines in the NIR are considerably blended, so for clarity we only mark the most dominant species for each feature (Mazzali et al. 2015; Dhawan et al. 2018; Diamond et al. 2018; Hoefflich et al. 2021). A more comprehensive set of identifications and a detailed list of strong NIR transitions from 0.8 to 2.4 μm can be found in Table 2, and associated figures from Diamond et al. (2018) and additional model line transitions in this region are given by Flörs et al. (2020) and Hoefflich et al. (2021).

Comparison to a dereddened ($R_V = 1.4$, $E(B-V) = 1.2$ mag; Amanullah et al. 2014; Foley et al. 2014; Mazzali et al. 2015), scaled Gemini North (GN) GNIRS (Elias et al. 2006, 2006)

spectrum of SN 2014J at the closest available phase of +289d (Diamond et al. 2018; Graur et al. 2020) and a dereddened ($E(B-V) = 0.023$ mag; Mazzali et al. 2015), scaled Large Binocular Telescope LUCIFER (Seifert et al. 2003) spectrum of SN 2011fe at similar phase of +234d shows good agreement between the SNe, with nearly all of the same lines present. The line strengths vary; though this may be attributed to the differences in phase. The NIR spectral features are predominantly blends of forbidden-line emission from the iron-group elements Fe, Co, and Ni. The [Ni I], [Ni II], and [Ni III] transitions are of particular interest for constraining models; however, none of the NIR nickel lines are isolated.

Between 2.5 and 5.0 μm , the NIR spectrum shows weak features, apart from two prominent features at around 2.9 μm and 3.2 μm , shown in Figure 4 and Figure 5. The peak flux of the feature at 2.9 μm is about half that of the 3.2 μm feature and is dominated by two strong [Fe III] lines at 2.874 and 2.905 μm . The red side of the peak may be blended with weaker [Ni II] 2.911 μm and [Fe III] 3.044 μm (Flörs et al. 2020).

The broad, somewhat-boxy feature centered near 3.2 μm is attributable to the [Ni I] 3.120 μm line on the blue side and the [Fe III] 3.229 μm line on the red side. Other potential blended contributors include [Fe III] 3.044 μm , [Co II] 3.286 μm , and [Co II] 3.151 μm lines. Models by Hoefflich et al. (2021) predict the [Ni I] 3.120 μm line to be strong and narrow, with the [Fe III] 3.229 μm line being weaker but broader. Our data suggest that the [Fe III] 3.229 μm line is indeed broader, but more detailed modeling of all potential lines in this region is needed to unambiguously determine line strengths in this blended feature. We further discuss the line profile shapes and measurements of the 3.2 μm feature in Section 4.1.1.

The remainder of the 2.5–5.0 μm region shows only unidentifiable weak lines and strong, isolated lines do not reappear until the MIR around 6.5 μm . Small bumps in the spectrum at ~ 3.4 μm ($S/N \simeq 9$) and ~ 3.8 μm ($S/N \simeq 8$) might be attributable to [Fe II] 3.393 μm and [Ni III] 3.802 μm , respectively, or a blend of unidentifiable features. Interestingly, several lines that are predicted to be strong do not appear in our JWST/NIRSpec observations of SN 2021aefx. Models from Hoefflich et al. (2021) predict strong [Fe II] 4.076 and 4.115 μm lines, and while there may be a small bump in the data in this region, it is weak ($S/N \simeq 7$). These models also predict weaker lines of [Co I] 2.526 μm and [Co I] 3.633 μm that we do not see strongly in our data. However, the models from Hoefflich et al. (2021) were made for a subluminous SN, so it may be expected that the ionization state and relative line strengths are different between the models and our data. Additionally, the [Co III] 3.492 μm line has been expected to contribute to the flux in the Spitzer CH1 (3.6 μm) photometric band (e.g., see Gerardy et al. 2007; Johansson et al. 2017); however, it does not appear in our NIR spectrum.

3.2. MIR Emission Lines

Starting from the MIR line identifications by Gerardy et al. (2007) for SN 2005df, we mark the dominant emission lines in the JWST/MIRI spectrum of SN 2021aefx in Figure 6. Compared with the Spitzer/intensified Reticon spectrograph (IRS) MIR spectra of SN 2005df and SN 2003hv (+117 and +359 rest-frame days from B_{max} , respectively; Gerardy et al. 2007), as well as an unpublished Spitzer spectrum of SN 2006ce (+127 rest-frame days from B_{max} ; Blackman et al. 2006; PID: 30292, PI: P. Meikle) downloaded from the

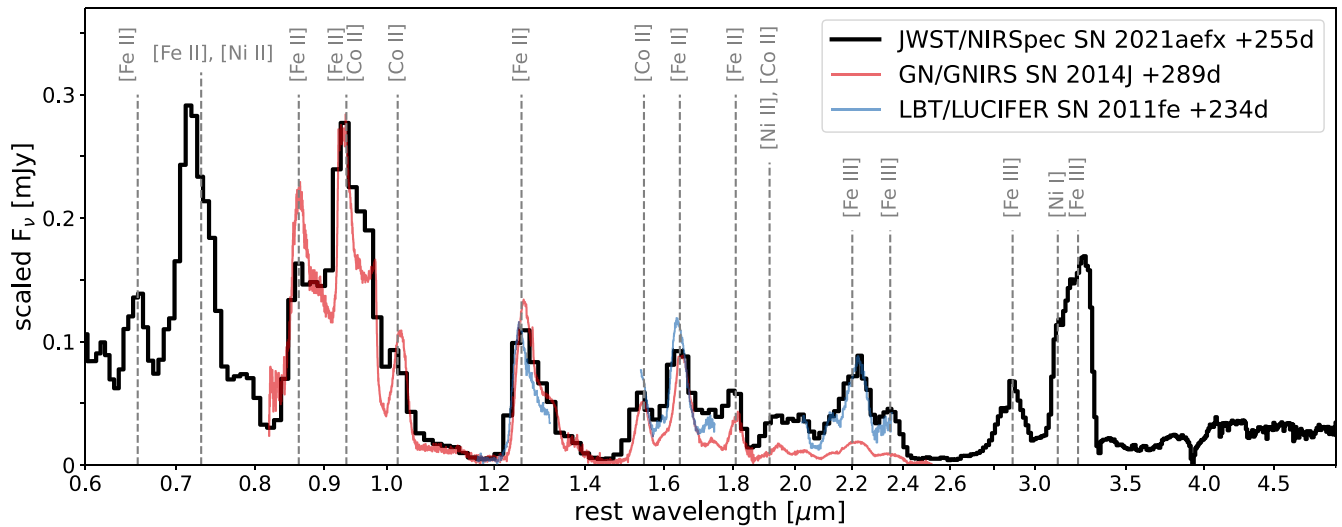


Figure 4. NIR line identifications for SN 2021aefx; only the most dominant species for each feature are shown. We compare the JWST/NIRSpec spectrum of SN 2021aefx (black) at +255 days with a scaled GN/GNIRS spectrum of SN 2014J (red) at the closest available phase of +289 days (Diamond et al. 2018; Graur et al. 2020) and a scaled LBT/LUCIFER JHK_s spectrum of SN 2011fe (blue) at a phase of +234 days (Mazzali et al. 2015). Nearly all emission lines are from significantly blended iron-group elements. The 2.5–5 μm region shows two strong blended features of predominantly [Fe III] 2.874 and 2.905 μm , and [Ni I] 3.120 μm and [Fe III] 3.229 μm , and several weak features. All spectra have been dereddened. Details of the NIR lines can be found in Table 2.

CASSIS database⁵² (Lebouteiller et al. 2011), and the GTC/CanariCam MIR spectrum of SN 2014J (+121 rest-frame days from B_{max} ; Telesco et al. 2015), the improvement in signal-to-noise ratio (S/N) of the JWST spectrum is striking. Despite differences in phase, the MIR spectra all show fairly close agreement, with the same major emission lines present but varying in strength and shape. The JWST/MIRI spectrum reveals additional, weaker emission lines and helps to confirm and clarify noisy lines in the Spitzer/IRS and GTC/CanariCam spectra. Details of our MIR line identifications can be found in Table 2.

The optical and NIR nebular spectra are dominated by iron-group elements with most of the strongest lines attributed to Fe emission, while the most dominant emission lines in the MIR instead come from Co and Ni. Prominent emission lines from Ar, an intermediate-mass element, also emerge in the MIR, providing new physical insight into the SN emission structure. These MIR emission lines are significantly less blended than those in the NIR, making their identification and subsequent fitting easier.

3.2.1. Iron-group Elements: Cobalt and Nickel

The brightest MIR feature is the isolated [Co III] 11.888 μm line, which shows close agreement with the SN 2005df and SN 2003hv spectra. The [Co II] 10.521 μm line is also fairly strong, and its peak is clearly resolved, although its base is blended with other lines on both sides. This line is potentially indistinguishably blended with the weaker and very nearby [S IV] 10.510 μm line (Gerardy et al. 2007). [Co II] 10.521 μm has roughly 25% the strength of the [Co III] 11.888 μm line, suggesting that there is comparatively little [Co II] emission.

On the blue side, the [Co II] 10.521 μm line is blended with a previously unidentified line, which creates a shoulder feature. We tentatively suggest that this unidentified line near 10.2 μm is [Fe II] 10.189 μm , [Fe III] 10.201 μm , or a combination of both. This shoulder feature is also visible in SN 2003hv and

potentially as a single pixel excess in SN 2005df; though it is not present in SN 2006ce or SN 2014J. It was not previously identified by Gerardy et al. (2007) due to high spectral noise.

The broad curve redward of the [Co II] 10.521 μm line exhibits two distinct bumps, indicating blended emission. We identify the expected strong [Ni III] 11.002 μm line and tentatively identify the weaker [Ni II] 10.682 μm line as the main contributing species. Weak [Co II] 11.167 μm emission may also broaden the redder of the two bumps, which is predominantly [Ni III] 11.002 μm . Inspection of the SN 2005df spectrum reveals a single pixel excess at the location of the bluer bump; the SN 2003hv spectrum also shows a peak (although without the JWST/MIRI spectrum for comparison, these very faint signals look like, and could be, noise). SN 2014J clearly exhibits two distinct peaks in this region while the SN 2006ce spectrum looks smoothly blended into one peak. All of the SNe exhibit emission consistent with the [Ni III] 11.002 μm line.

The second brightest MIR feature, at roughly 50% of the [Co III] 11.888 μm line strength, is the relatively isolated [Ni III] 7.349 μm line. This feature in SN 2021aefx is slightly weaker in relative strength than those in SN 2006ce and SN 2003hv, but is stronger than that in SN 2005df.

The [Ni IV] 8.405 μm line in SN 2021aefx has a roughly equal peak flux as the neighboring [Ar III] 8.991 μm line and is fairly well isolated, with minimal blending. This line was identified for SN 2005df; though its strength was only about 30% the strength of the [Ar III] 8.991 μm line. SN 2006ce and SN 2014J also exhibit the [Ni IV] 8.405 μm line, and like SN 2021aefx, it has roughly equal peak flux to the [Ar III] 8.991 μm line. The [Ni IV] feature in SN 2003hv was only speculatively identified by Gerardy et al. (2007) due to noise, but it is confirmed more clearly when compared to the MIRI spectrum of SN 2021aefx.

While Gerardy et al. (2007) found no convincing detection of the [Ni II] 6.636 μm line (partially due to excess noise in the 7.4 μm region from the overlapping edges of spectral orders), our JWST/MIRI spectrum displays a clear “shoulder” feature

⁵² <https://cassis.sirtf.com/>

Table 2
Line Identification and Fitting for SN 2021aefx^a

λ_{rest} (μm)	Species	Fit Profile	λ_{peak} (μm)	v_{peak} (km s^{-1})	FWHM (km s^{-1})	Transition	A_{ki}	E_{lu} (eV)
Optical + NIR Lines								
0.589	[Co III]	Gaussian	0.591	1000 \pm 500	10,800 \pm 2500	$a^4F_{9/2} - a^2G_{9/2}$	4.20×10^{-1}	0.000–2.105
0.716	[Fe II]	Gaussian	0.717	600 \pm 100	8900 \pm 2200	$a^4F_{9/2} - a^2G_{9/2}$	1.46×10^{-1}	0.232–1.964
0.738	[Ni II]	Gaussian	0.740	900 \pm 200	9700 \pm 3600	$^2D_{5/2} - ^2F_{7/2}$	2.30×10^{-1}	0.000–1.680
1.257	[Fe II]	Gaussian	1.263	1300 \pm 1500	9400 \pm 1500	$a^6D_{9/2} - a^4D_{7/2}$	4.74×10^{-03}	0.000–0.986
1.547	[Co II]	Gaussian	1.545	–400 \pm 1300	jussi6100 \pm 2200	a^5F_5, b^3F_4	2.81×10^{-02}	0.415–1.217
1.644	[Fe II]	Gaussian	1.651	1300 \pm 1200	11,100 \pm 2400	$a^4F_{9/2} - a^4D_{7/2}$	6.00×10^{-03}	0.232–0.986
1.939	[Ni II]	Gaussian	1.949	300 \pm 1000	11,300 \pm 1000	$^4F_{9/2} - ^2F_{7/2}$	8.70×10^{-02}	1.041–1.680
2.219	[Fe III]	Gaussian	2.226	1100 \pm 800	9900 \pm 800	$^3H_6 - ^3G_5$	3.40×10^{-02}	2.486–3.045
2.874	[Fe III]	Gaussian	2.867	–100 \pm 500	13,900 \pm 4300	$^3F_4 - ^3G_4$	2.70×10^{-02}	2.661–3.092
2.905	[Fe III]	Gaussian	2.906			$^3F_4 - ^3G_3$	2.90×10^{-02}	2.690–3.117
3.120	[Ni I]	Gaussian	3.118	–200 \pm 400	6300 \pm 1900	$^3D_3 - ^1D_2$	7.80×10^{-02}	0.025–0.423
3.229	[Fe III]	Gaussian	3.209	–1900 \pm 400	11,300 \pm 3000	$^3F_4 - ^3G_5$	1.70×10^{-02}	2.661–3.045
MIR Lines								
6.636	[Ni II]	Gaussian	6.725	4000 \pm 1500	12,000 \pm 3500	$^2D_{5/2} - ^2D_{3/2}$	5.54×10^{-02}	0.000–0.187
6.985	[Ar II]	Gaussian	7.084	4000 \pm 1500	20,500 \pm 4100	$^2P_{3/2}^o - ^2P_{1/2}^o$	4.23×10^{-02}	0.000–0.177
7.349	[Ni III]	Gaussian	7.422	3000 \pm 1400	11,200 \pm 1300	$^3F_4 - ^3F_3$	6.50×10^{-02}	0.000–0.169
8.405	[Ni IV]	Sphere	8.447	1300 \pm 1200	13,600 \pm 600	$^4F_{9/2} - ^4F_{7/2}$	5.70×10^{-02}	0.000–0.148
8.991	[Ar III]	Shell	9.012	700 \pm 1100	23,700 \pm 600	$^3P_2 - ^3P_1$	3.10×10^{-02}	0.000–0.138
10.521	[Co II]	Gaussian	10.562	1200 \pm 1000	8300 \pm 1300	a^3F_4, a^3F_3	2.24×10^{-02}	0.000–0.118
11.002	[Ni III]	Gaussian	11.051	1300 \pm 900	10,700 \pm 2400	$^3F_3 - ^3F_2$	2.70×10^{-02}	0.169–0.281
11.888	[Co III]	Gaussian	11.911	500 \pm 900	10,200 \pm 1300	$a^4F_{9/2} - a^4F_{7/2}$	2.01×10^{-02}	0.000–0.104
Tentative Lines								
2.911	[Ni II]?	Gaussian	2.913	4800 \pm 2000	–400 \pm 2600	$^4F_{5/2} - ^2F_{7/2}$	1.40×10^{-02}	1.254–1.680
3.044	[Fe III]?	$^3F_4 - ^3G_3$	1.80×10^{-02}	2.710–3.117
3.286	[Co II]?	Gaussian	3.287	–300 \pm 400	5900 \pm 1200	c^3F_4, a^1F_3	1.86×10^{-03}	5.089–5.467
6.214	[Co II]?	a^1D_2, a^3P_2	3.08×10^{-02}	1.445–1.644
6.920	[Ni II]?	Gaussian	7.055	5800 \pm 2000	12,000 \pm 4000	$^2F_{7/2} - ^2F_{5/2}$	4.71×10^{-02}	1.680–1.859
6.985	[Ar II]?	Shell	7.039	2300 \pm 1500	23,700 \pm 600	$^2P_{3/2}^o - ^2P_{1/2}^o$	4.23×10^{-02}	0.000–0.177
7.791	[Fe III]?	$^3P_4 - ^3P_4$	4.70×10^{-02}	2.406–2.565
10.189	[Fe II]?	Gaussian	10.235	1000 \pm 1000	6700 \pm 1700	$b^4P_{5/2} - b^4P_{3/2}$	2.30×10^{-02}	2.583–2.704
10.201	[Fe III]?	$^3H_4 - ^3F_4$	1.60×10^{-03}	2.539–2.661
10.510	[S IV]?	$^2P_{1/2}^o - ^2P_{3/2}^o$	7.30×10^{-03}	0.000–0.118
10.682	[Ni II]?	Gaussian	10.842	4500 \pm 1000	4200 \pm 1500	$^4F_{9/2} - ^4F_{7/2}$	2.71×10^{-02}	1.041–1.157
11.167	[Co II]?	Gaussian	11.214	1300 \pm 900	3100 \pm 1400	b^3F_4, b^3F_3	1.88×10^{-02}	1.217–1.328
12.002	[Ni I]?	\sim 1500	...	$^3D_2 - ^3D_1$	2.10×10^{-02}	0.109–0.212
12.729	[Ni II]?	$^4F_{7/2} - ^4F_{5/2}$	2.76×10^{-02}	1.157–1.254

Note.

^a Line information from the Atomic Line List version 3.00b4.

on the blue side of the 7–8 μm region explained by [Ni II] 6.636 μm blending with the nearby [Ar II] 6.985 μm line.

Further analysis of these iron-group element features in the MIR spectrum is given in Section 4.2 and Section 4.3, where we fit simple geometric line profiles and estimate kinematic properties for each identified line.

3.2.2. Intermediate-mass Elements: Sulfur and Argon

[S IV] 10.510 μm line emission theoretically contributes to the [Co II] 10.521 μm peak (Gerardy et al. 2007); however, it is too closely blended, and our spectral resolution is too low for direct identification or further analysis, especially given the additional blending with Ni on both sides. Detailed theoretical models will be needed to disentangle the contribution of [S IV] 10.510 μm .

Two important argon emission lines appear in the MIR. In the MIRI spectrum, the [Ar III] 8.991 μm line is only slightly blended with the [Ni IV] 8.405 μm line. We see a broad, well-resolved flat-topped profile indicative of a lack of emission at low projected velocities implying a spherical shell of emission. This boxy [Ar III] shape differs significantly from the forked [Ar III] and [Ar II] profiles that Gerardy et al. (2007) found for both SN 2005df and SN 2003hv, attributed to an asymmetric ring of emission. SN 2006ce and SN 2014J appear to have an asymmetrically sloped [Ar III] profile, highlighting interesting differences in the distribution of argon between these SNe.

Visible as a small bump on top of the broad blue wing of the [Ni III] 7.349 μm feature, the [Ar II] 6.985 μm line in SN 2021aefx is nearly completely blended into the Ni emission lines that surround it. With such strong blending, it is difficult to conclusively determine the shape of this line; we further

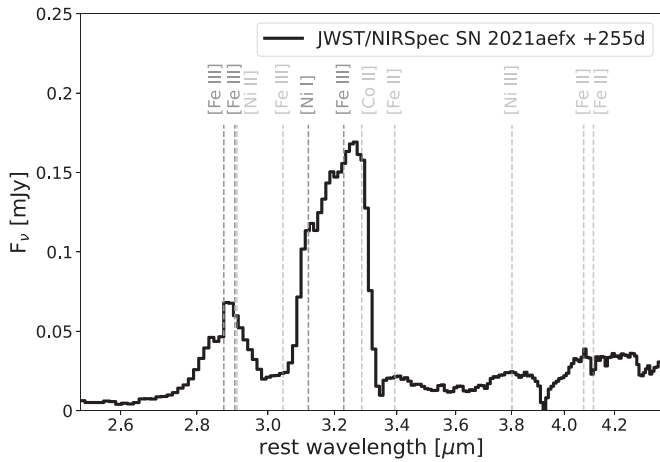


Figure 5. JWST/NIRSpec line identifications in the $3\ \mu\text{m}$ region, previously unobserved for SN Ia. The main line features arise from [Fe III] 2.874 and $2.905\ \mu\text{m}$, and [Ni II] $3.120\ \mu\text{m}$ and [Fe III] $3.229\ \mu\text{m}$ emission (gray). Several possible weaker lines that may be blended with the dominant lines are shown in light gray. Details of the dominant lines can be found in Table 2.

analyze the shape of the [Ar III] $8.991\ \mu\text{m}$ and [Ar II] $8.405\ \mu\text{m}$ lines and discuss their implications in Section 4.4.

3.2.3. Unidentified and Speculative Features

Gerardy et al. (2007) suggest possible detection of silicon monoxide (SiO) molecular emission in the $\sim 7.5\text{--}8\ \mu\text{m}$ region of SN 2005df, corresponding to the fundamental ($\Delta_v = 1$) rovibrational band. Hoefflich et al. (1995) concluded that CO and SiO might form in subluminescent SNe Ia with very low ^{56}Ni yield, and SN 2005df was a subluminescent SN Ia, making detection of SiO an interesting possibility. However, SN 2021aefx is a normal SN Ia; furthermore, our full NIR + MIR spectrum does not show convincing evidence for CO or SiO fundamental emission elsewhere in the spectrum. Thus, we favor an explanation for the weak emission feature at $\sim 7.8\ \mu\text{m}$ by [Fe III] $7.791\ \mu\text{m}$, which is predicted by models from Flörs et al. (2020).

We speculate that the faint emission feature at $\sim 6.2\ \mu\text{m}$ is [Co II] $6.214\ \mu\text{m}$. [Ni II] $12.729\ \mu\text{m}$ may be detected redward of the strong [Co III] $11.888\ \mu\text{m}$ line, but an increase in noise toward the end of the spectrum prevents conclusive detection. Finally, a small spike on top of the red side of the [Co III] $11.888\ \mu\text{m}$ peak is tentative evidence for [Ni I] $12.001\ \mu\text{m}$.

4. Line Velocities and Profiles

At late times in the nebular phase, the SN ejecta opacity drops, and emission streams freely from all regions, revealing important properties of the ejecta composition and ionization structure. The shape of the nebular emission lines is determined by the ejecta emissivity, which depends on both the density and excitation (for a review, see Jerkstrand 2017). Several simple ejecta geometries that produce common line profiles include a uniform sphere resulting in a parabolic shape, a uniform spherical thick shell resulting in a boxy, flat-topped shape with parabolic wings, and a Gaussian density sphere resulting in a Gaussian line profile (Jerkstrand 2017). The MIR, where the features are comparatively isolated, is particularly useful for inferring the kinematic distribution of the emission.

Most of the lines that we identify can be well modeled by a superposition of Gaussian line profiles. Using the +266 days

emission line model of SN 2015F from Flörs et al. (2020), and following the approach of Maguire et al. (2018) and Flörs et al. (2018, 2020), we model the superposition of all [Fe II], [Fe III], [Ni II], [Co II], and [Co III] lines contributing to selected optical and NIR features. The relative line strengths of each line are fixed by the model, and all lines of the same species are restricted to have the same Gaussian width and kinematic offset from the central wavelength. Because this model was computed for temperatures and densities specific to SN 2015F, not SN 2021aefx, we do not attempt to fit the entire optical or NIR spectrum, but rather fit the model to selected regions containing features of interest.

Past $3\ \mu\text{m}$, the emergence of lines from species not included in the SN 2015F model from Flörs et al. (2020) prevents us from modeling each feature in such a thorough and self-consistent way. Furthermore, the model relative line strengths begin to deviate significantly from the data for the NIR $3.2\ \mu\text{m}$ feature and the MIR. Thus, we fit each feature redward of $3\ \mu\text{m}$ as a superposition of basic geometric line-emission profiles for each distinguishable contributing line, allowing the amplitude, kinematic offset, and width of each individual line to be free parameters. Fit profile shapes for each line are chosen based upon visual inspection of best overall feature fit. A proper, bespoke model for SN 2021aefx is beyond the scope of this paper, but will be the focus of future effort.

We use UltraNest (Buchner 2021), a Bayesian inference package for parameter estimation using nested sampling, to fit our line profiles and recover uncertainties on our measurements of kinematic offset (v_{peak}) and full width half maximum. The likelihood function optimized in the UltraNest fitting is given by the following:

$$\ln(\text{likelihood}) = -\frac{1}{2} \sum \left[\frac{(\text{data} - \text{model})^2}{s^2} + \ln(2\pi s^2) \right],$$

where

$$s^2 = \text{data_uncertainty}^2 + f^2 \text{model}^2;$$

and the uncertainties are underestimated by some fractional amount f that is marginalized over in the fit. For the MIR lines, we include a systematic uncertainty in the wavelength calibration of $0.034\ \mu\text{m}$, derived from the root mean square of the wavelength calibration residuals in the region encompassing the SN features ($6.5\text{--}12.5\ \mu\text{m}$), and add this in quadrature to the kinematic offset uncertainties. The typically low resolution of our data results in instrumental broadening ($c\Delta\lambda/\lambda$) that is significant: $\sim 4500\ \text{km s}^{-1}$ at $1.25\ \mu\text{m}$ and $\sim 1000\ \text{km s}^{-1}$ at $3.3\ \mu\text{m}$ for the NIR, and $\sim 1900\ \text{km s}^{-1}$ at $6.5\ \mu\text{m}$ and $\sim 450\ \text{km s}^{-1}$ at $12\ \mu\text{m}$ for the MIR. We remove this in quadrature from our FWHM measurements and impose a floor on our line centroid uncertainty equal to one-third the instrumental resolution. For a sense of scale, the instrumental resolution is roughly 50% of the FWHM of the [Co III] $1.257\ \mu\text{m}$ line, 10% of the FWHM of the [Fe III] $3.229\ \mu\text{m}$ line, 15% of the FWHM of the [Ni III] $7.349\ \mu\text{m}$ line, and 5% of the FWHM of the [Co III] $11.889\ \mu\text{m}$ line.

Our line fits do not include any radiative transfer, and we only attempt basic accounting of line blending by superposition. Table 2 gives the chosen fit profile shape, measured peak wavelength, kinematic offset, FWHM, and the estimated uncertainties of each fitted feature.

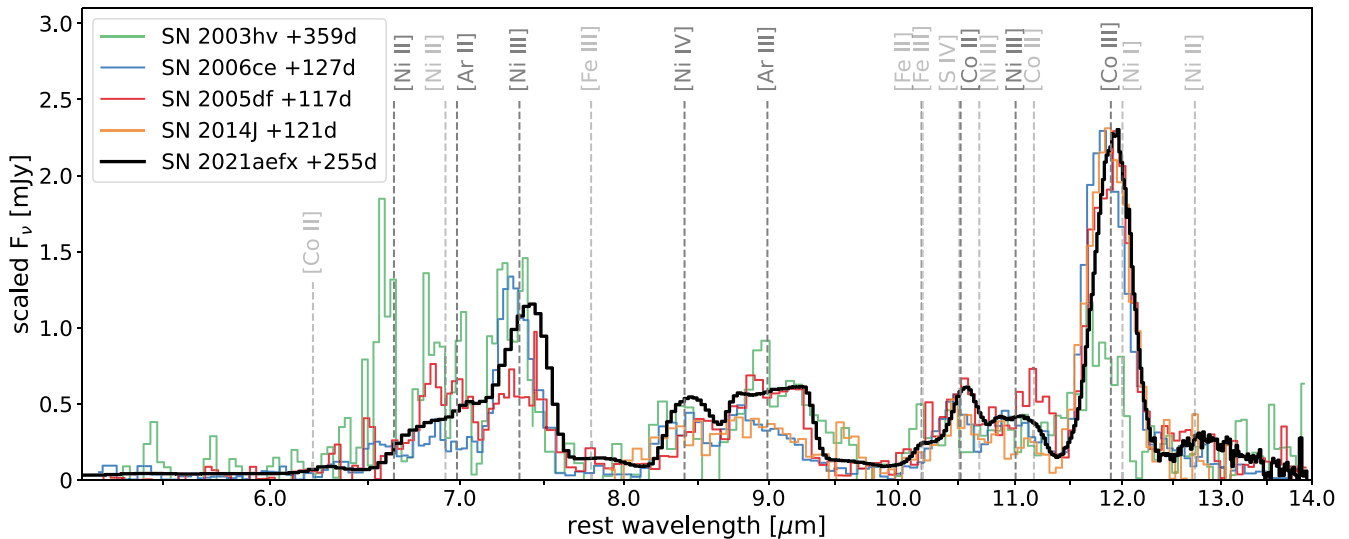


Figure 6. MIR line identifications for our JWST/MIRI spectrum of SN 2021aefx (black) at +255 days. We compare to scaled Spitzer/IRS MIR spectra of SN 2005df (red) at +117 days and SN 2003hv (green) at +359 days (Gerardy et al. 2007), SN 2006ce (blue) +127 days, and a MIR spectrum from GTC/CanariCam of SN 2014J (orange) at +121 days (Telesco et al. 2015). All phases are given in rest-frame days relative to B_{\max} . The JWST/MIRI spectrum shows impressive improvement in S/N, allowing for additional identification of weaker lines. The dominant emission lines are marked in gray, with uncertain line identifications marked in light gray. Details of the MIR lines can be found in Table 2.

4.1. Optical + NIR: Iron and Nickel

Using the SN 2015F model from Flörs et al. (2020) as described above, we fit the NIR [Fe II] 1.257 μm , [Fe II] 1.644 μm , and [Fe III] 2.218 μm features, shown in Figure 7. We find agreement within the uncertainties, in both v_{peak} and FWHM, between all of these lines, which exhibit a moderately redshifted v_{peak} .

Like the models by Maguire et al. (2018), the SN 2015F model from Flörs et al. (2020) only contains significant line contributions in the 1.3 μm region from [Fe II], as shown in Figure 7. The model fits the data well in this region, and the measured FWHM and v_{peak} agree closely with those measured from the optical [Fe II] 0.716 μm and NIR [Fe II] 1.644 μm lines. This supports the conclusion of Maguire et al. (2018) that the 1.3 μm feature is a relatively contaminant free way to measure line velocities and widths for [Fe II].

We also fit the optical 7300 \AA line complex of [Fe II] 0.716 μm and [Ni II] 0.738 μm with the SN 2015F model, as shown in Figure 7. The measured FWHM and v_{peak} for the [Fe II] 0.716 μm line are within the uncertainties of the NIR Fe lines. The [Ni II] 0.738 μm line is consistent in FWHM with the other [Ni II] and [Ni III] lines in the NIR and MIR. Its v_{peak} is comparable to [Ni II] 1.939 μm , [Ni III] 11.002 μm , and [Ni IV] 8.405 μm , but lower than [Ni II] 6.644 μm and [Ni III] 7.349 μm , which may be partly attributed to the imperfect JWST MIRI/LRS wavelength calibration that is worse at the shorter wavelengths. Overall, from the optical 7300 \AA line complex, the [Fe II] 0.716 μm and [Ni II] 0.738 μm kinematics are roughly consistent with the Fe and Ni kinematics from the NIR and MIR.

We detect the [Ni II] 1.939 μm line feature in our NIR spectrum, shown in Figure 10, which has also been seen in other ground-based studies of the NIR (Dhawan et al. 2018; Flörs et al. 2020; Blondin et al. 2022). Fitting this feature with the 2015F model, we find an FWHM that is comparable to the FWHM of Ni II in the MIR. The v_{peak} is within the uncertainties of the [Ni II] 0.738 μm , [Ni III] 7.349 μm , [Ni III] 11.00 μm , and [Ni IV] 8.41 μm lines and slightly

smaller than the [Ni II] 6.64 μm v_{peak} , again possibly affected by the MIR wavelength calibration.

Following Flörs et al. (2020), we find that, while we cannot rule out weak [Ca II] line contamination in the 7300 \AA line complex, strong [Ca II] contamination in the optical would require a weaker [Ni II] 0.716 μm line, thus predicting a weaker [Ni II] 1.939 μm line because no [Ca II] is present there. Our fits to [Ni II] 0.738 μm and [Ni II] 1.939 μm have similar amplitudes, and we do not see a weaker [Ni II] 1.939 μm line than expected from [Ni II] 0.738 μm . Thus, in agreement with the findings by Maguire et al. (2018) and Flörs et al. (2020), we do not find a compelling reason to invoke contamination from [Ca II] to reconcile the differences in kinematic properties between the optical and NIR + MIR.

4.1.1. NIR: 2.9 and 3.2 μm Features

The [Fe III] 2.874 μm + [Fe III] 2.905 μm line feature, fit to the SN 2015F model from Flörs et al. (2020), has contributions from [Ni II] 2.911 μm and [Fe III] 3.044 μm , shown in Figure 8. This feature exhibits a broad FWHM consistent with [Fe III] 2.218 μm and [Fe III] 3.229 μm , and a blueshifted v_{peak} between the other two NIR [Fe III] lines.

We fit the feature at 3.2 μm with a superposition of three Gaussian emission distribution profiles, shown in Figure 8. The strongest lines expected in this feature are [Ni I] 3.120 μm and [Fe III] 3.229 μm , but to improve the fit of the full feature, we include a third [Co II] 3.286 μm line. This fit produces a strong, broad [Fe III] 3.229 μm line consistent in FWHM with [Fe III] 2.874 μm and [Fe III] 2.218 μm , but with a large blueshifted v_{peak} . This may indicate that a more comprehensive model is needed to explain the 3.2 μm feature. The fits to the [Ni I] 3.120 μm and [Co II] 3.286 μm lines show weaker, narrower profiles of similar strength, FWHM, and low kinematic offset.

Alternatively, we can fit the 3.2 μm feature nearly equally well without [Co II] 3.286 μm , but it requires boxy, flat-topped profiles for both [Ni I] 3.120 μm and [Fe III] 3.229 μm . In this alternative fit, both lines are of similar strengths, nearly equally broad, and display large redshifts. However, these profiles

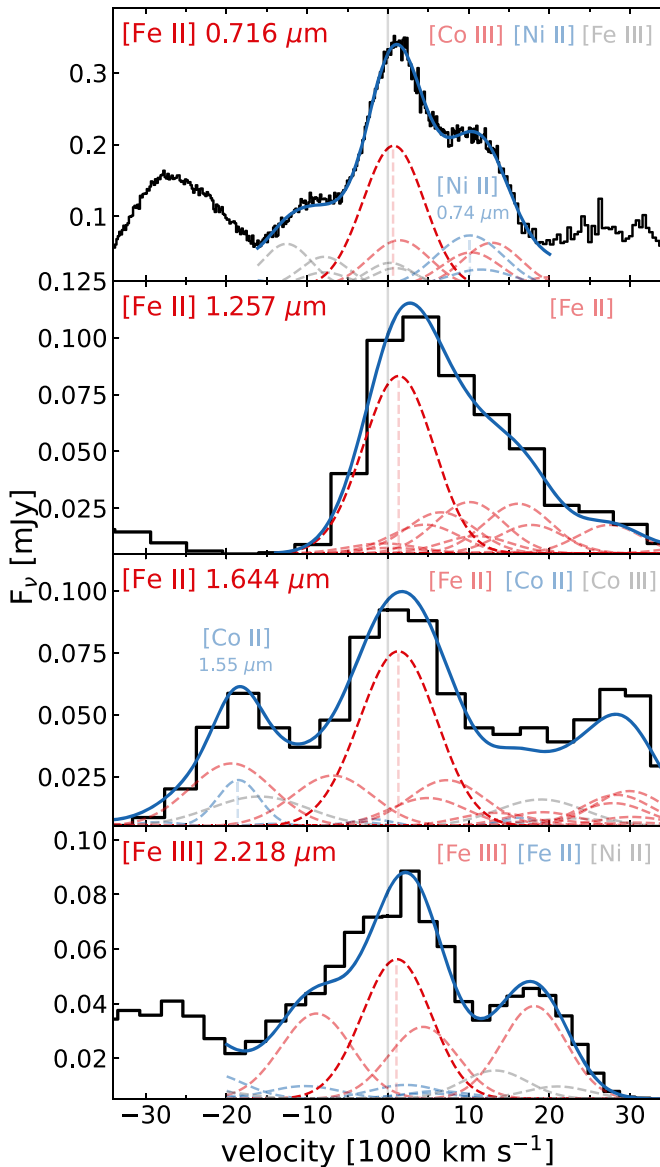


Figure 7. Optical + NIR emission-line profiles of SN 2021aefx at +255 days (black) for complex spectral features dominated by iron. The model profile for the central line is shown in dashed red, with contributions from other lines shown in dashed light red and dashed light blue, and the full modeled superposition of lines shown in solid blue.

would imply a large central hole of both [Fe III] and [Ni I] emission that would be difficult to explain physically. The Fe comes from ^{56}Ni decay and is expected to be broad, whereas the observed Ni must be stable ^{58}Ni , as all radioactive ^{56}Ni has decayed away at this phase. The stable Ni is expected to be centrally concentrated and thus with a narrower, peaked profile. Furthermore, flat-topped profiles are not seen in other Ni and Fe features throughout the optical, NIR, and MIR spectra. Therefore, we favor the Gaussian profile fits with inclusion of an unexpectedly strong [Co II] 3.286 μm line. More detailed future modeling of this feature may reveal additional contributing lines.

4.2. MIR: Cobalt

Shown in Figure 9, the [Co III] 11.888 μm line is well fit by a fairly broad Gaussian profile and low kinematic offset from the

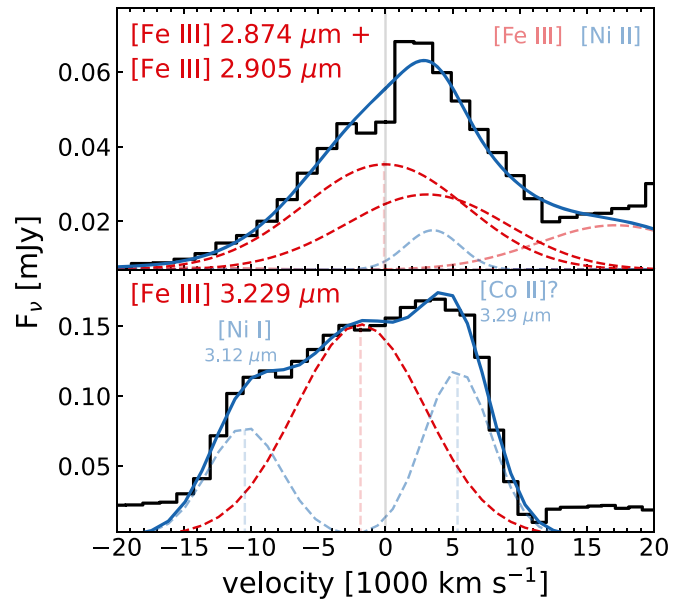


Figure 8. NIR emission-line profiles of SN 2021aefx at +255 days (black) for the 3 μm region features. The model profile for the central line is shown in dashed red, with contributions from other lines shown in dashed blue and the full modeled superposition of lines shown in solid blue.

host-galaxy rest frame. Gerardy et al. (2007) find evidence for a parabolic, slightly flat-topped [Co III] 11.888 μm profile for SN 2005df resulting from a spherical distribution with a hollow inner region, and a significantly blueshifted, fairly flat, and weak [Co III] 11.888 μm line for SN 2003hv. SN 2021aefx shows a Gaussian [Co III] distribution with clear wings not expected from a uniform spherical distribution. However, close inspection of the Gaussian fit shows that the peak may be marginally flat-topped, potentially indicating a Gaussian distribution with a small central hole corresponding to the electron capture zone where little Co is produced (Gerardy et al. 2007).

The [Co II] 10.521 μm line is blended so closely with the predicted weaker [S IV] 10.510 μm line that they are indistinguishable, and we model them as one line. We model the full blended $\sim 10\text{--}11.3$ μm feature as a linear combination of five Gaussians: [Fe II] 10.189 μm /[Fe III] 10.201 μm , [Co II] 10.521 μm , [Ni II] 10.682 μm , [Ni III] 11.002 μm , and [Co II] 11.167 μm . The FWHM, v_{peak} , and Gaussian profile shape agree nicely between the [Co III] 11.888 μm and [Co II] 10.521 μm lines.

For comparison to the optical and NIR, we also fit the SN 2015F model from Flörs et al. (2020) to the [Co III] 0.589 μm and [Co III] 1.547 μm lines in Figure 9. The [Co II] and [Co III] measurements agree quite well across the optical, NIR, and MIR, and we conclude that the emission structure between Co ionization states is similar; though the MIR line strengths suggest there is less emission from [Co II]. The tentative identifications of [Co II] 11.167 μm and [Co II] 3.286 μm show decent agreement as well; though they are significantly less broad and slightly blueshifted, respectively.

4.3. MIR: Nickel

The SN 2021aefx MIR nickel emission-line profiles, shown in Figure 10, are all blended with other emission-line profiles, with the [Ni IV] 8.405 μm and [Ni III] 7.349 μm lines being the most isolated. Despite blending, the JWST/MIRI Ni lines in

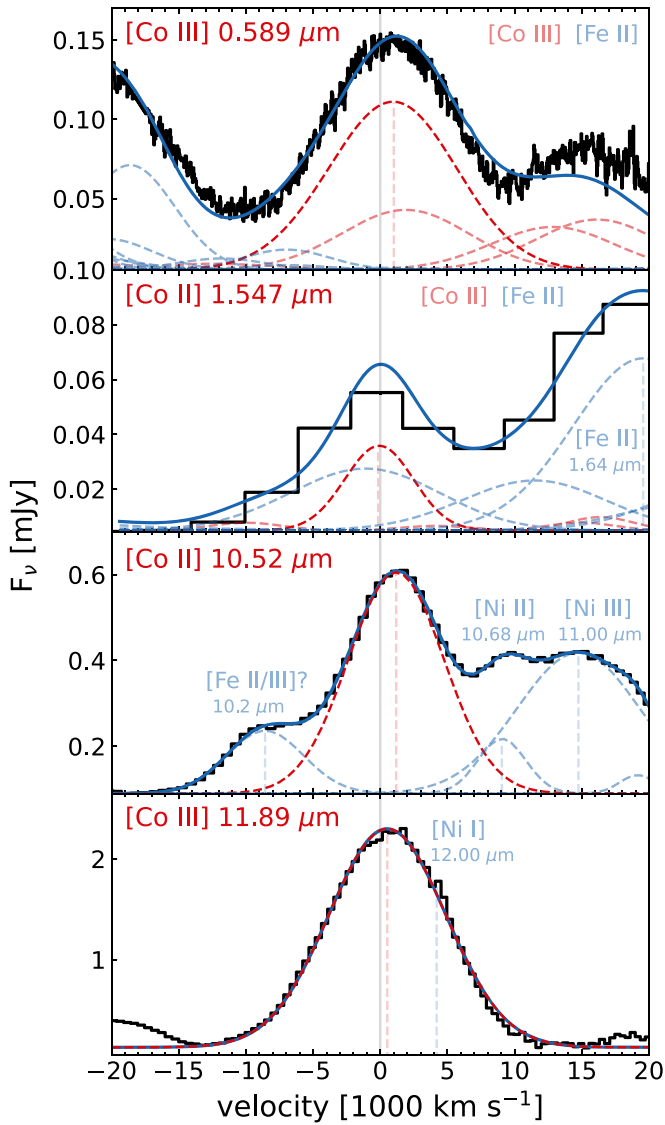


Figure 9. Cobalt emission-line profiles of SN 2021aefx at +255 days (black) across the optical, NIR, and MIR compared with model line emission from Gaussian distributions of emission. The model profile for the central line is shown in dashed red, with contributions from other lines shown in dashed blue and the full modeled superposition of lines shown in solid blue.

SN 2021aefx are significantly better resolved than the Spitzer/IRS and GTC/CanariCam spectra, and we can fit the blended Ni lines well by Gaussian profiles, except for [Ni IV] 8.405 μm , which prefers a parabolic profile. The wings of a Gaussian profile for [Ni IV] 8.405 μm contribute too much to the boxy [Ar III] 8.991 μm feature, implying the [Ni IV] emission arises from a uniform spherical, rather than Gaussian, geometry.

The Ni lines show significantly redshifted kinematic offsets, except for neutral [Ni I] 3.120 μm , which is also the only NIR Ni line that we fit. [Ni II] 6.636 μm and [Ni III] 7.349 μm exhibit the highest v_{peak} values, which may be partially due to the MIRI wavelength solution being more uncertain at shorter wavelengths. Taking the wavelength uncertainties into account, these lines are within the uncertainty range of the [Ni IV] 8.405 μm and [Ni III] 11.002 μm measurements. These MIR [Ni II] and [Ni III] lines are consistent in FWHM, while the NIR [Ni I] 3.120 μm line is narrower. The tentatively identified [Ni II] 10.682 μm line shows a highly redshifted v_{peak} , consistent

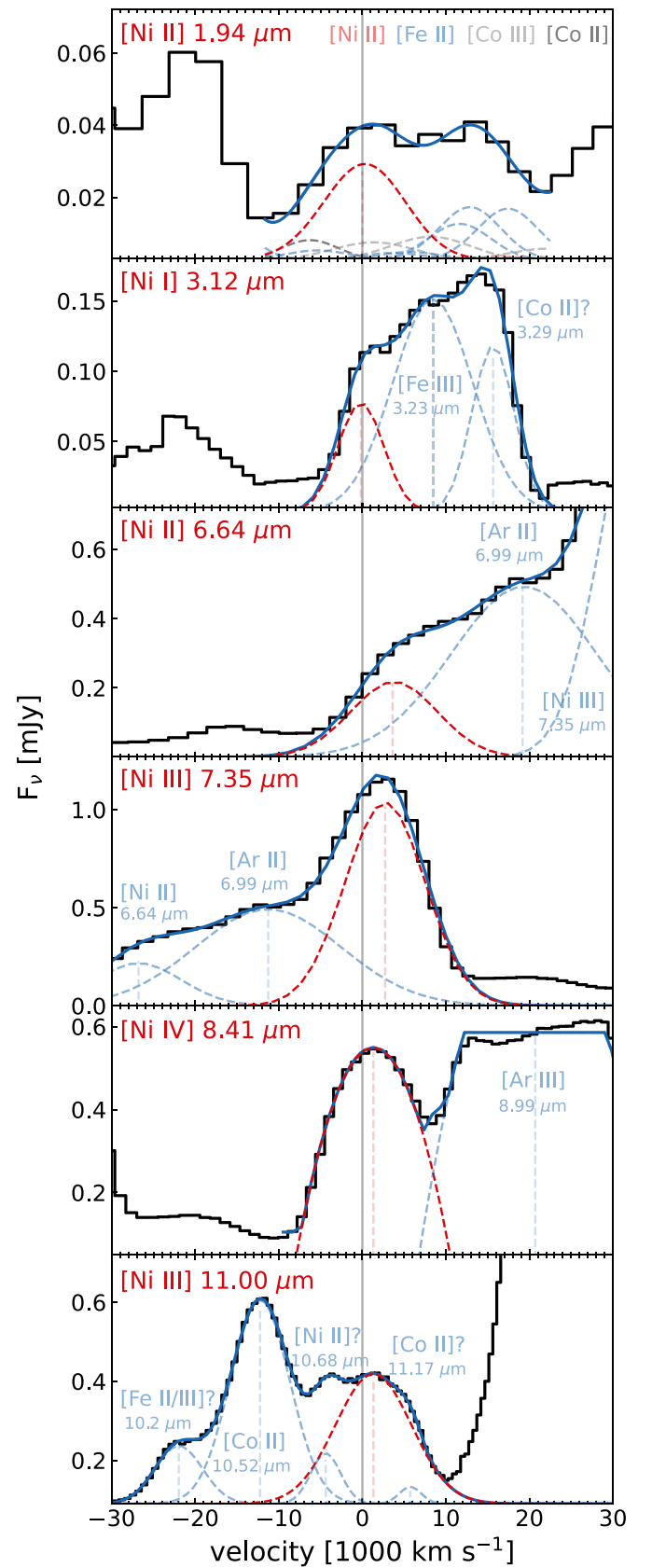


Figure 10. Observed NIR and MIR nickel emission-line profiles for SN 2021aefx at +255 days (black) compared to model line emission from Gaussian distributions of emission, except for [Ni IV] 8.405 μm , which is better fit by emission from a uniform spherical emission distribution. The model profile for the central line is shown in dashed red, with contributions from other lines shown in dashed blue and the full modeled superposition of lines shown in solid blue.

with [Ni II] 6.636 μm and [Ni III] 7.349 μm , but with an inconsistently narrower FWHM.

4.4. MIR: Argon

Appearing only in the MIR, the argon lines reveal new structure in the SN emission. Gerardy et al. (2007) find that the [Ar II] 6.985 μm and [Ar III] 8.991 μm lines have distinctive forked profiles in both SN 2005df and SN 2003hv, indicating an asymmetric, ring-shaped argon distribution. In contrast, for SN 2021aefx, the [Ar III] 8.991 μm feature in SN 2021aefx has a very distinctive boxy shape, indicative of a hollow uniform sphere, or thick shell, of emission.

Shown in Figure 11, [Ar III] 8.991 μm has a very broad FWHM $\approx 23,700 \text{ km s}^{-1}$, with an inner shell radius corresponding to a minimum velocity of $v_{\text{min}} = 8700 \pm 200 \text{ km s}^{-1}$, and an outer radius corresponding to $v_{\text{max}} = 13,500 \pm 300 \text{ km s}^{-1}$. The flat-top of the [Ar III] 8.991 μm line is only slightly sloped and is more symmetric than in the other SNe observed by Spitzer and GTC/CanariCam. Indeed, the [Ar III] 8.991 μm line shape exhibits considerable variation across the SNe in Figure 6.

The [Ar II] 6.985 μm feature in SN 2021aefx is heavily blended on both sides by [Ni II] 6.636 μm and [Ni III] 7.349 μm , making it difficult to conclusively determine its geometry. We find that the full $\sim 6.5\text{--}7.5 \mu\text{m}$ feature is well fit by a sum of three Gaussian profiles, with the Gaussian representing [Ar II] 6.985 μm having a very broad FWHM $\approx 20,600 \text{ km s}^{-1}$, and high redshifted $v_{\text{peak}} \approx 4000 \text{ km s}^{-1}$. However, most lines from the same element share similar shapes, and we can fit the feature equally well with a boxy, shell profile for [Ar II] 6.985 μm if we include an additional line, which could be [Ni II] 6.920 μm . In Figure 11, we show a fit to the [Ar II] 6.895 μm line where we force it to have the same inner and outer shell radii as the [Ar III] 8.991 μm fit. This forced fit reduces v_{peak} of [Ar II] but yields a very high redshifted $v_{\text{peak}} \approx 5800 \text{ km s}^{-1}$ for [Ni II] 6.920 μm . Without the boxy [Ar III] profile, we would not consider a boxy profile for [Ar II], and the fit is not unique because we could allow the [Ar II] shell to have different radial boundaries than those of [Ar III]. More detailed modeling of this feature is needed to fully disentangle the profile of [Ar II]. We further discuss the shapes of the Ar lines and their implications in Section 5.

5. Summary and Conclusions

We present nebular SN Ia NIR and MIR spectra of SN 2021aefx from JWST, including the first observation of the 2.5–5 μm region and the highest S/N MIR SN Ia spectrum to date.

At the phase of our observations (+255 days), all of the radioactive ^{56}Ni has decayed away, and the Ni emission lines that we see come from stable ^{58}Ni . We unambiguously detect stable Ni in the ejecta of SN 2021aefx via the strong [Ni I] 3.120 μm and [Ni II] 7.349 μm lines, a clearly resolved [Ni IV] 8.405 μm line, and several other weaker, blended Ni lines. Electron capture reactions producing stable iron-group elements require high-density burning above $\sim 10^8 \text{ g cm}^{-3}$ that is found in carbon–oxygen white dwarfs with $M \gtrsim 1.2 M_{\odot}$ (Hoefflich et al. 1996; Iwamoto et al. 1999; Seitzzahl et al. 2013; Hoefflich et al. 2017; Seitzzahl & Townsley 2017). The strong detection of stable Ni advocates for a massive, perhaps near-Chandrasekhar mass, progenitor for SN 2021aefx.

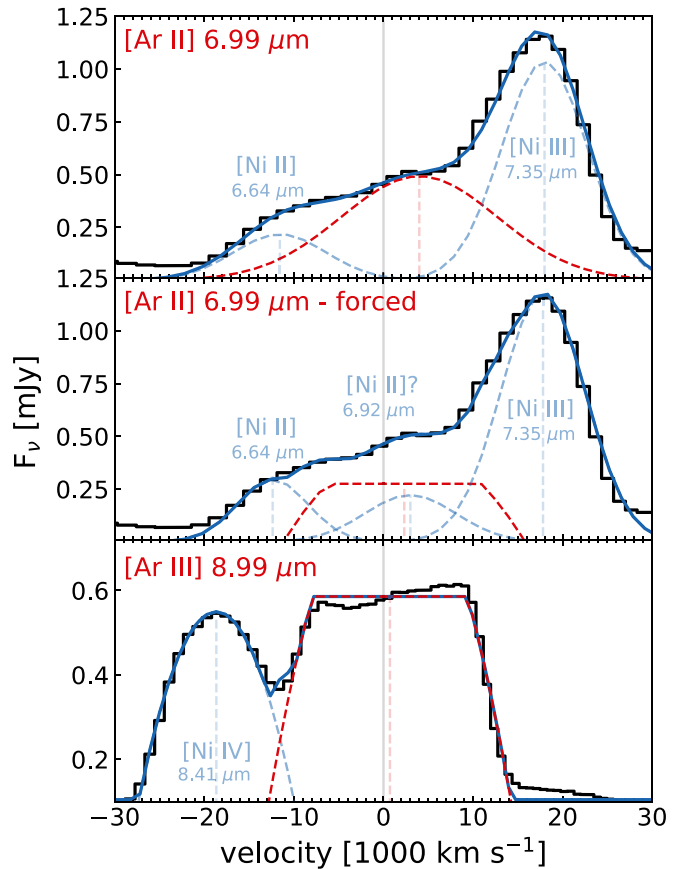


Figure 11. Observed argon emission-line profiles for SN 2021aefx at +255 days (black) compared to model line emission from a Gaussian emission distribution for [Ar II] 6.985 μm (top); a thick uniform shell or hollow uniform sphere emission distribution for [Ar III] 8.991 μm with an inner radius corresponding to $v_{\text{min}} = 8700 \pm 200 \text{ km s}^{-1}$, and an outer radius corresponding to $v_{\text{max}} = 13,500 \pm 300 \text{ km s}^{-1}$ (bottom); and a thick shell distribution for [Ar II] 6.985 μm , which has been forced to have the same inner and outer radius as the [Ar III] fit (middle). The model profile for the central line is shown in dotted red, with contributions from other lines shown in dotted blue and the full modeled superposition of lines shown in solid blue.

However, our relatively low instrumental resolution does not allow us to probe the ejecta structure at the lowest velocities (the central region), and a more detailed quantitative analysis is needed to determine whether the stable nickel mass could be consistent with a lower-mass progenitor in a double-detonation scenario (Flörs et al. 2020; Blondin et al. 2022).

We fit emission-line profiles to prominent NIR and MIR lines to investigate their kinematic properties and geometric emission distributions. As shown in Figure 12, the iron-group elements (Fe, Co, and Ni) largely cluster around a redshifted kinematic offset of $\sim 1000 \pm 1000 \text{ km s}^{-1}$ and an FWHM of $\sim 11,000 \pm 4000 \text{ km s}^{-1}$. We find consistent kinematic offsets between the Co lines, with [Co III] having a slightly higher FWHM than [Co II], hinting that it may extend out to larger radii. This could indicate recombination in the higher-density central region. McClelland et al. (2013) suggested that the more rapid decline seen in Spitzer IRAC photometry of SN 2011fe at 3.6 μm compared to 4.5 μm could also be a result of recombination of doubly ionized species in the 3.6 μm band; indeed, our data show [Fe III] emission should dominate that region.

The Ni lines have a slightly higher overall redshifted kinematic offset than those of Co and Fe. However, we caution

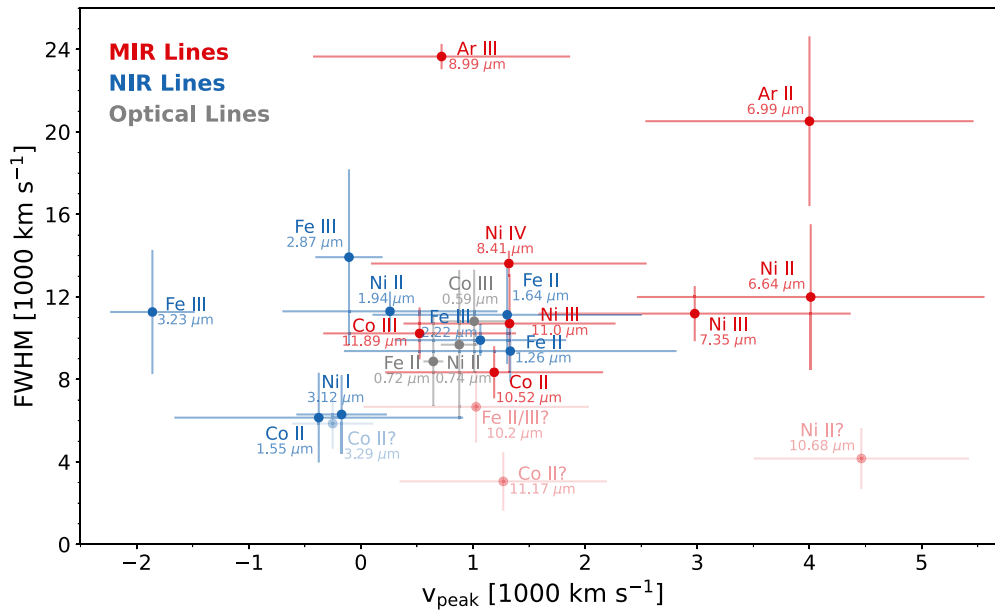


Figure 12. FWHM vs. kinematic offset for species with fitted line profiles in Section 4. MIR lines (red) are compared against NIR lines (blue) and optical lines (gray). Error bars show fit uncertainties, in combination with wavelength calibration uncertainties for the MIR lines, and take into account instrument resolution. Low opacity points represent uncertain line identifications. Values and errors for these measurements are given in Table 2.

that the largest redshifted kinematic offsets are found at the shortest MIRI wavelengths where the calibration is most uncertain.

The reliably identified Fe lines are all consistent in FWHM. The [Fe III] $3.229 \mu\text{m}$ line, which was not modeled with the SN 2015F model from Flörs et al. (2020) like the other NIR Fe lines, is significantly blueshifted in kinematic offset compared to the other Fe lines; more detailed future modeling of this feature may bring it into closer agreement with the other Fe line measurements. Comparing the width of the [Fe II] $1.644 \mu\text{m}$ line ($\sim 12,000 \text{ km s}^{-1}$) to the models for SN 2014J from (Diamond et al. 2018; e.g., see Figure 9), we find that SN 2021aefx has a higher central density than that of SN 2014J. Although the uncertainties are large, there is a slight hint that a redshifted kinematic offset is seen for [Fe II] compared to [Fe III]; as described by Maeda et al. (2010), the low-ionization lines trace the deflagration ash, and this may be a signature of a delayed-detonation explosion where the initial deflagration produces an offset innermost ejecta while the subsequent detonation creates a spherically symmetric outer ejecta.

The argon lines are significantly broader than those of the iron-group elements, implying that argon extends to higher velocities, and correspondingly, radii. This result may support detonation models that produce stratified ejecta from nucleosynthesis in the low-density outer layers leading to intermediate-mass elements, and nucleosynthesis in the high-density interior producing the iron-group elements (Khokhlov 1991; Woosley & Weaver 1994; Wiggins et al. 1998; Fink et al. 2007; Sim et al. 2010).

The flat-topped shape of the [Ar III] $8.991 \mu\text{m}$ line indicates a thick shell geometry for the [Ar III] emission, which could be produced by either a physical lack of Ar in the central regions or a lack of doubly ionized Ar in the interior. The [Ni IV] $8.405 \mu\text{m}$ line, which has an ionization energy of 35.2 eV, has a smooth parabolic profile suggesting that [Ni IV] is present in the central region. Based just on ionization energies, it should then be possible to doubly ionize argon to [Ar III], which

requires 27.6 eV, in the center. This would argue for a physical absence of Ar in the innermost ejecta, a flat-topped profile for [Ar II], and a stratified ejecta from a detonation. Comparison of ionization energies is likely too simplistic; indeed, Fransson & Jerkstrand (2015) show that at late times in the high-density regions, a large fraction of the energy comes from ionizations and excitations, rather than just thermal heating. A detailed future analysis should explore whether [Ni IV] can be formed in the central region without central emission of [Ar III].

Overall, the Gaussian, parabolic, and flat-topped shapes of the fit profiles for SN 2021aefx point to spherically symmetric distributions of emission for all species. This is consistent with the low level of continuum polarization of SNe Ia during the photospheric phase, as strong asymmetry of the radioactive distribution will lead to directional dependence of polarization (Wang & Wheeler 2008; Yang et al. 2022). More JWST MIR data of SNe Ia will improve our understanding of asymmetry in the explosions.

More detailed analyses, such as the derivation of elemental abundances and inferred masses, and modeling of this and future JWST data of SN 2021aefx will be the subject of future work. Continuing observations of SN 2021aefx with JWST will build a time series of four epochs of JWST spectra and will be the most comprehensive SN Ia nebular IR data set available. As part of JWST cycle (1) GO program 2072 (PI: S. W. Jha), another NIRSpec/Prism + MIRI/LRS spectrum will be obtained roughly 100 days after the first, and two additional MIRI spectra of SN 2021aefx will be obtained through JWST cycle (1) GO program 2114 (PI: C. Ashall), including planned MIRI medium-resolution spectrometer (MRS) spectroscopy doubling the wavelength range out to $28 \mu\text{m}$, with higher spectral resolution. The analysis of SN 2021aefx over time will reveal the evolution of radioactivity, ionization, and density structure of the ejecta.

SN 2021aefx is an excellent first reference SN Ia for JWST observations, and the initial analysis that we present here highlights the promise of JWST to be transformative for the study of nebular phase SN Ia.

We thank Shelly Meyett for her consistently excellent work scheduling these JWST observations, Greg Sloan for assistance with the MIRI LRS wavelength solution correction, and Glenn Wahlgren for help with the NIRSpec observations.

This work is based on observations made with the NASA/ESA/CSA JWST. The data were obtained from the Mikulski Archive for Space Telescopes at the Space Telescope Science Institute, which is operated by the Association of Universities for Research in Astronomy, Inc., under NASA contract NAS 5-03127 for JWST. These observations are associated with JWST program No. 02072. Support for this program at Rutgers University was provided by NASA through grant JWST-GO-02072.001.

The SALT data presented here were obtained with Rutgers University program 2022-1-MLT-004 (PI: Jha). We are grateful to SALT Astronomer Rosalind Skelton for taking these observations.

L.A.K. acknowledges support by NASA FINESST fellowship 80NSSC22K1599.

T.S. is supported by the NKFIH/OTKA FK-134432 grant of the National Research, Development and Innovation (NRDI) Office of Hungary, the János Bolyai Research Scholarship of the Hungarian Academy of Sciences, and the New National Excellence Program (ÚNKP-22-5) of the Ministry for Innovation and Technology of Hungary from the source of NRDI Fund.

Time-domain research by the University of Arizona team and D.J.S. is supported by NSF grants AST-1821987, 1813466, 1908972, and 2108032, and by the Heising-Simons Foundation under grant No. 2020-1864.

K.M. acknowledges support from the Japan Society for the Promotion of Science (JSPS) KAKENHI grants JP18H05223 and JP20H00174.

L.G. acknowledges financial support from the Spanish Ministerio de Ciencia e Innovación (MCIN), the Agencia Estatal de Investigación (AEI) 10.13039/501100011033, and the European Social Fund (ESF) “Investing in your future” under the 2019 Ramón y Cajal program RYC2019-027683-I and the PID2020-115253GA-I00 HOSTFLOWS project, from Centro Superior de Investigaciones Científicas (CSIC) under the PIE project 20215AT016, and the program Unidad de Excelencia María de Maeztu CEX2020-001058-M.

K.M. and M.D. are funded by the EU H2020 ERC grant No. 758638.

J.P.H. acknowledges support from the George A. and Margaret M. Downs brough bequest.

The Aarhus supernova group is funded in part by an Experiment grant (No. 28021) from the Villum FONDEN, and by a project (1) grant (No. 8021-00170B) from the Independent Research Fund Denmark (IRFD).

C.L. acknowledges support from the National Science Foundation Graduate Research Fellowship under grant No. DGE-2233066.

A.F. acknowledges support by the European Research Council (ERC) under the European Union’s Horizon 2020 research and innovation program (ERC advanced grant KILO-NOVA No. 885281).







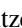


Facilities: JWST, SALT.

Software: Astropy (Astropy Collaboration et al. 2018), Matplotlib (Hunter 2007), NumPy (Harris et al. 2020), PyRAF (Science Software Branch at STScI 2012), PySALT (Crawford et al. 2010), dust extinction (Gordon et al. 2022), jdaviz

(JDADF Developers et al. 2022), jwst (Bushouse et al. 2022), UltraNest (Buchner 2021; Buchner et al. 2022).

ORCID iDs

Lindsey A. Kwok  <https://orcid.org/0000-0003-3108-1328>
 Saurabh W. Jha  <https://orcid.org/0000-0001-8738-6011>
 Tea Temim  <https://orcid.org/0000-0001-7380-3144>
 Ori D. Fox  <https://orcid.org/0000-0003-2238-1572>
 Conor Larison  <https://orcid.org/0000-0003-2037-4619>
 Yssavo Camacho-Neves  <https://orcid.org/0000-0002-9830-3880>
 Max J. Brenner Newman  <https://orcid.org/0000-0002-8092-2077>
 Justin D. R. Pierel  <https://orcid.org/0000-0002-2361-7201>
 Ryan J. Foley  <https://orcid.org/0000-0002-2445-5275>
 Jennifer E. Andrews  <https://orcid.org/0000-0003-0123-0062>
 Carles Badenes  <https://orcid.org/0000-0003-3494-343X>
 Barnabas Barna  <https://orcid.org/0000-0003-4769-4794>
 K. Azalee Bostroem  <https://orcid.org/0000-0002-4924-444X>
 Maxime Deckers  <https://orcid.org/0000-0001-8857-9843>
 Andreas Flörs  <https://orcid.org/0000-0003-2024-2819>
 Peter Garnavich  <https://orcid.org/0000-0003-4069-2817>
 Melissa L. Graham  <https://orcid.org/0000-0002-9154-3136>
 Or Graur  <https://orcid.org/0000-0002-4391-6137>
 Griffin Hosseinzadeh  <https://orcid.org/0000-0002-0832-2974>
 D. Andrew Howell  <https://orcid.org/0000-0003-4253-656X>
 John P. Hughes  <https://orcid.org/0000-0002-8816-6800>
 Joel Johansson  <https://orcid.org/0000-0001-5975-290X>
 Sarah Kendrew  <https://orcid.org/0000-0002-7612-0469>
 Wolfgang E. Kerzendorf  <https://orcid.org/0000-0002-0479-7235>
 Keiichi Maeda  <https://orcid.org/0000-0003-2611-7269>
 Kate Maguire  <https://orcid.org/0000-0002-9770-3508>
 Curtis McCully  <https://orcid.org/0000-0001-5807-7893>
 John T. O’Brien  <https://orcid.org/0000-0003-3615-9593>
 Armin Rest  <https://orcid.org/0000-0002-4410-5387>
 David J. Sand  <https://orcid.org/0000-0003-4102-380X>
 Melissa Shahbandeh  <https://orcid.org/0000-0002-9301-5302>
 Louis-Gregory Strolger  <https://orcid.org/0000-0002-7756-4440>
 Tamás Szalai  <https://orcid.org/0000-0003-4610-1117>
 Chris Ashall  <https://orcid.org/0000-0002-5221-7557>
 E. Baron  <https://orcid.org/0000-0001-5393-1608>
 Chris R. Burns  <https://orcid.org/0000-0003-4625-6629>
 James M. DerKacy  <https://orcid.org/0000-0002-7566-6080>
 Tyco Mera Evans  <https://orcid.org/0000-0001-5888-2542>
 Alec Fisher  <https://orcid.org/0000-0002-5253-3584>
 Lluís Galbany  <https://orcid.org/0000-0002-1296-6887>
 Peter Hoeflich  <https://orcid.org/0000-0002-4338-6586>
 Eric Hsiao  <https://orcid.org/0000-0003-1039-2928>
 Thomas de Jaeger  <https://orcid.org/0000-0001-6069-1139>
 Emir Karamehmetoglu  <https://orcid.org/0000-0001-6209-838X>
 Kevin Krisciunas  <https://orcid.org/0000-0002-6650-694X>
 Sahana Kumar  <https://orcid.org/0000-0001-8367-7591>
 Jing Lu  <https://orcid.org/0000-0002-3900-1452>
 Justyn Maund  <https://orcid.org/0000-0003-0733-7215>
 Paolo A. Mazzali  <https://orcid.org/0000-0001-6876-8284>

Kyle Medler  <https://orcid.org/0000-0001-7186-105X>
 Nidia Morrell  <https://orcid.org/0000-0003-2535-3091>
 Mark. M. Phillips  <https://orcid.org/0000-0003-2734-0796>
 Benjamin J. Shappee  <https://orcid.org/0000-0003-4631-1149>
 Maximilian Stritzinger  <https://orcid.org/0000-0002-5571-1833>
 Nicholas Suntzeff  <https://orcid.org/0000-0002-8102-181X>
 Charles Telesco  <https://orcid.org/0000-0002-0036-9292>
 Michael Tucker  <https://orcid.org/0000-0002-2471-8442>
 Lifan Wang  <https://orcid.org/0000-0001-7092-9374>

References

- Allison, J. R., Sadler, E. M., & Meekin, A. M. 2014, *MNRAS*, **440**, 696
 Amanullah, R., Goobar, A., Johansson, J., et al. 2014, *ApJL*, **788**, L21
 Ashall, C., Lu, J., Shappee, B. J., et al. 2022, *ApJL*, **932**, L2
 Astropy Collaboration, Price-Whelan, A. M., Sipőcz, B. M., et al. 2018, *AJ*, **156**, 123
 Averbukh, J., Bradley, L., et al. 2022, Jdaviz, v3.1.0, Zenodo, doi:10.5281/zenodo.7255461, JDADF Developers
 Axelrod, T. S. 1980, PhD thesis, Univ. California, Santa Cruz
 Birkmann, S. M., Giardino, G., Sirianni, M., et al. 2022, *Proc. SPIE*, **12180**, 121802P
 Black, C. S., Fesen, R. A., & Parrent, J. T. 2016, *MNRAS*, **462**, 649
 Blackman, J., Schmidt, B., & Kerzendorf, W. 2006, *CBET*, **541**, 1
 Blondin, S., Bravo, E., Timmes, F. X., Dessart, L., & Hillier, D. J. 2022, *A&A*, **660**, A96
 Blondin, S., Matheson, T., Kirshner, R. P., et al. 2012, *AJ*, **143**, 126
 Bostroem, K. A., Jha, S. W., Randriamampandry, S., et al. 2021, *TNSCR*, **2021-3888**
 Bowers, E. J. C., Meikle, W. P. S., Geballe, T. R., et al. 1997, *MNRAS*, **290**, 663
 Branch, D., Jeffery, D. J., Parrent, J., et al. 2008, *PASP*, **120**, 135
 Brown, T. M., Baliber, N., Bianco, F. B., et al. 2013, *PASP*, **125**, 1031
 Buchner, J. 2021, *JOSS*, **6**, 3001
 Buchner, J., Ball, W., Smirnov-Pinchukov, G., Nitz, A., & Susemihl, N. 2022, JohannesBuchner/UltraNest: v3.5.0, Zenodo, doi:10.5281/zenodo.7053560
 Burns, C., Hsiao, E., Suntzeff, N., et al. 2021, *ATel*, **14441**, 1
 Bushouse, H., Eisenhamer, J., Dencheva, N., et al. 2022, JWST Calibration Pipeline, v1.7.0, doi:10.5281/zenodo.7038885
 Childress, M. J., Hillier, D. J., Seitzzahl, I., et al. 2015, *MNRAS*, **454**, 3816
 Crawford, S. M., Still, M., Schellart, P., et al. 2010, *Proc. SPIE*, **7737**, 25
 Dalcanton, J. J., Williams, B. F., Seth, A. C., et al. 2009, *ApJS*, **183**, 67
 Dhawan, S., Flörs, A., Leibundgut, B., et al. 2018, *A&A*, **619**, A102
 Diamond, T. R., Hoeflich, P., Hsiao, E. Y., et al. 2018, *ApJ*, **861**, 119
 Elias, J. H., Joyce, R. R., Liang, M., et al. 2006, *Proc. SPIE*, **6269**, 62694C
 Elias, J. H., Rodgers, B., Joyce, R. R., et al. 2006, *Proc. SPIE*, **6269**, 626914
 Fink, M., Hillebrandt, W., & Röpke, F. K. 2007, *A&A*, **476**, 1133
 Fink, M., Röpke, F. K., Hillebrandt, W., et al. 2010, *A&A*, **514**, A53
 Fitzpatrick, E. L., Massa, D., Gordon, K. D., Bohlin, R., & Clayton, G. C. 2019, *ApJ*, **886**, 108
 Flörs, A., Spyromilio, J., Maguire, K., et al. 2018, *A&A*, **620**, A200
 Flörs, A., Spyromilio, J., Taubenberger, S., et al. 2020, *MNRAS*, **491**, 2902
 Foley, R. J., Fox, O. D., McCully, C., et al. 2014, *MNRAS*, **443**, 2887
 Fransson, C., & Jerkstrand, A. 2015, *ApJL*, **814**, L2
 Friesen, B., Baron, E., Wisniewski, J. P., et al. 2014, *ApJ*, **792**, 120
 Gerardy, C. L., Meikle, W. P. S., Kotak, R., et al. 2007, *ApJ*, **661**, 995
 Goobar, A., Johansson, J., Amanullah, R., et al. 2014, *ApJL*, **784**, L12
 Gordon, K., Larson, K., McBride, A., et al. 2022, karllark/dust_extinction: NIRspectralExtinctionAdded, v1.1, Zenodo, doi:10.5281/zenodo.6397654
 Gordon, K. D., Misselt, K. A., Bouwman, J., et al. 2021, *ApJ*, **916**, 33
 Graham, M. L., Kennedy, T. D., Kumar, S., et al. 2022, *MNRAS*, **511**, 3682
 Graur, O., Maguire, K., Ryan, R., et al. 2020, *NatAs*, **4**, 188
 Harris, C. R., Millman, K. J., van der Walt, S. J., et al. 2020, *Natur*, **585**, 357
 Hoeflich, P., Ashall, C., Bose, S., et al. 2021, *ApJ*, **922**, 186
 Hoeflich, P., Chakraborty, S., Comaskey, W., et al. 2017, *MmSAI*, **88**, 302
 Hoeflich, P., Khokhlov, A., Wheeler, C. J., et al. 1996, *ApJL*, **472**, L81
 Hoeflich, P., Khokhlov, A. M., & Wheeler, J. C. 1995, *ApJ*, **444**, 831
 Hosseinzadeh, G., & Gomez, S. 2020, Light Curve Fitting, v0.2.0, Zenodo, doi:10.5281/zenodo.4312178
 Hosseinzadeh, G., Sand, D. J., Lundqvist, P., et al. 2022, *ApJL*, **933**, L45
 Hunter, J. D. 2007, *CSE*, **9**, 90
 Iwamoto, K., Brachwitz, F., Nomoto, K., et al. 1999, *ApJS*, **125**, 439
 Jakobsen, P., Ferruit, P., Alves de Oliveira, C., et al. 2022, *A&A*, **661**, A80
 Jerkstrand, A. 2017, in Handbook of Supernovae, ed. A. W. Alsabti & P. Murdin (Cham: Springer)
 Johansson, J., Goobar, A., Kasliwal, M. M., et al. 2017, *MNRAS*, **466**, 3442
 Kalari, V. M., Vink, J. S., Dufton, P. L., et al. 2014, *A&A*, **564**, L7
 Kendrew, S., Scheithauer, S., Bouchet, P., et al. 2015, *PASP*, **127**, 623
 Kendrew, S., Scheithauer, S., Bouchet, P., et al. 2016, *Proc. SPIE*, **9904**, 990443
 Khokhlov, A. M. 1991, *A&A*, **245**, 114
 Leboutteiller, V., Barry, D. J., Spoon, H. W. W., et al. 2011, *ApJS*, **196**, 8
 Maeda, K., Taubenberger, S., Sollerman, J., et al. 2010, *ApJ*, **708**, 1703
 Maguire, K., Sim, S. A., Shingles, L., et al. 2018, *MNRAS*, **477**, 3567
 Mazzali, P. A., Sullivan, M., Filippenko, A. V., et al. 2015, *MNRAS*, **450**, 2631
 McClelland, C. M., Garnavich, P. M., Milne, P. A., Shappee, B. J., & Pogge, R. W. 2013, *ApJ*, **767**, 119
 McCully, C., Turner, M., Volgenau, N., et al. 2018, LCOGT/Banzai: Initial Release, Zenodo, doi:10.5281/zenodo.1257560
 Nomoto, K., Thielemann, F. K., & Wheeler, J. C. 1984, *ApJL*, **279**, L23
 Pakmor, R., Kromer, M., Taubenberger, S., et al. 2012, *ApJL*, **747**, L10
 Rho, J., Kozasa, T., Reach, W. T., et al. 2008, *ApJ*, **673**, 271
 Rieke, G. H., Ressler, M. E., Morrison, J. E., et al. 2015, *PASP*, **127**, 665
 Rigby, J., Perrin, M., McElwain, M., et al. 2022, arXiv:2207.05632
 Sabbi, E., Calzetti, D., Ubeda, L., et al. 2018, *ApJS*, **235**, 23
 Schlafly, E. F., & Finkbeiner, D. P. 2011, *ApJ*, **737**, 103
 Science Software Branch at STScI 2012, PyRAF: Python Alternative for IRAF, Astrophysics Source Code Library, ascl:1207.011
 Seifert, W., Appenzeller, I., Baumeister, H., et al. 2003, *Proc. SPIE*, **4841**, 962
 Seitzzahl, I. R., & Townsley, D. M. 2017, in Handbook of Supernovae, ed. A. W. Alsabti & P. Murdin (Cham: Springer)
 Seitzzahl, I. R., Ciaraldi-Schoolmann, F., Röpke, F. K., et al. 2013, *MNRAS*, **429**, 1156
 Silverman, J. M., Nugent, P. E., Gal-Yam, A., et al. 2013, *ApJS*, **207**, 3
 Sim, S. A., Röpke, F. K., Hillebrandt, W., et al. 2010, *ApJL*, **714**, L52
 Smith, M. P., Nordsieck, K. H., Burgh, E. B., et al. 2006, *Proc. SPIE*, **6269**, 62692A
 Tartaglia, L., Sand, D. J., Valenti, S., et al. 2018, *ApJ*, **853**, 62
 Telesco, C. M., Höflich, P., Li, D., et al. 2015, *ApJ*, **798**, 93
 Thielemann, F. K., Nomoto, K., & Yokoi, K. 1986, *A&A*, **158**, 17
 Tiels, A. G. G. M. 2005, The Physics and Chemistry of the Interstellar Medium (Cambridge: Cambridge Univ. Press)
 Tucker, M. A., Ashall, C., Shappee, B. J., et al. 2022, *ApJL*, **926**, L25
 Valenti, S., Howell, D. A., Stritzinger, M. D., et al. 2016, *MNRAS*, **459**, 3939
 Wang, L. 2005, *ApJL*, **635**, L33
 Wang, L., & Wheeler, J. C. 2008, *ARA&A*, **46**, 433
 Wiggins, D. J. R., Sharpe, G. J., & Falle, S. A. E. G. 1998, *MNRAS*, **301**, 405
 Wilk, K. D., Hillier, D. J., & Dessart, L. 2020, *MNRAS*, **494**, 2221
 Woosley, S. E., & Weaver, T. A. 1994, *ApJ*, **423**, 371
 Wright, G. S., Wright, D., Goodson, G. B., et al. 2015, *PASP*, **127**, 595
 Yang, Y., Yan, H., Wang, L., et al. 2022, *ApJ*, **939**, 18